Micromechanics of Composite Materials Governed by Vector Constitutive Laws

Brett A. Bednarcyk
Glenn Research Center, Cleveland, Ohio

Jacob Aboudi
Tel Aviv University, Tel Aviv, Israel

Steven M. Arnold
Glenn Research Center, Cleveland, Ohio

NASA STI Program . . . in Profile

Since its founding, NASA has been dedicated to the advancement of aeronautics and space science. The NASA Scientific and Technical Information (STI) Program plays a key part in helping NASA maintain this important role.

The NASA STI Program operates under the auspices of the Agency Chief Information Officer. It collects, organizes, provides for archiving, and disseminates NASA's STI. The NASA STI Program provides access to the NASA Technical Report Server—Registered (NTRS Reg) and NASA Technical Report Server—Public (NTRS) thus providing one of the largest collections of aeronautical and space science STI in the world. Results are published in both non-NASA channels and by NASA in the NASA STI Report Series, which includes the following report types:

- TECHNICAL PUBLICATION. Reports of completed research or a major significant phase of research that present the results of NASA programs and include extensive data or theoretical analysis. Includes compilations of significant scientific and technical data and information deemed to be of continuing reference value. NASA counter-part of peer-reviewed formal professional papers, but has less stringent limitations on manuscript length and extent of graphic presentations.

- TECHNICAL MEMORANDUM. Scientific and technical findings that are preliminary or of specialized interest, e.g., "quick-release" reports, working papers, and bibliographies that contain minimal annotation. Does not contain extensive analysis.

- CONTRACTOR REPORT. Scientific and technical findings by NASA-sponsored contractors and grantees.

- CONFERENCE PUBLICATION. Collected papers from scientific and technical conferences, symposia, seminars, or other meetings sponsored or co-sponsored by NASA.

- SPECIAL PUBLICATION. Scientific, technical, or historical information from NASA programs, projects, and missions, often concerned with subjects having substantial public interest.

- TECHNICAL TRANSLATION. English-language translations of foreign scientific and technical material pertinent to NASA's mission.

For more information about the NASA STI program, see the following:

- Access the NASA STI program home page at http://www.sti.nasa.gov

- E-mail your question to help@sti.nasa.gov

- Fax your question to the NASA STI Information Desk at 757-864-6500

- Telephone the NASA STI Information Desk at 757-864-9658

- Write to:
  NASA STI Program
  Mail Stop 148
  NASA Langley Research Center
  Hampton, VA 23681-2199

Micromechanics of Composite Materials Governed by Vector Constitutive Laws

Brett A. Bednarcyk
Glenn Research Center, Cleveland, Ohio

Jacob Aboudi
Tel Aviv University, Tel Aviv, Israel

Steven M. Arnold
Glenn Research Center, Cleveland, Ohio

Acknowledgments

Level of Review: This material has been technically reviewed by technical management.

Available from

Micromechanics of Composite Materials
Governed by Vector Constitutive Laws

Brett A. Bednarcyk
National Aeronautics and Space Administration
Glenn Research Center
Cleveland, Ohio 44135

Jacob Aboudi
Tel Aviv University
Tel Aviv, Israel

Steven M. Arnold
National Aeronautics and Space Administration
Glenn Research Center
Cleveland, Ohio 44135

Abstract

The high-fidelity generalized method of cells micromechanics theory has been extended for the prediction of the effective property tensor and the corresponding local field distributions for composites whose constituents are governed by vector constitutive laws. As shown, the shear analogy, which can predict effective transverse properties, is not valid in the general three-dimensional case. Consequently, a general derivation is presented that is applicable to both continuously and discontinuously reinforced composites with arbitrary vector constitutive laws and periodic microstructures. Results are given for thermal and electric problems, effective properties and local field distributions, ordered and random microstructures, as well as complex geometries including woven composites. Comparisons of the theory's predictions are made to test data, numerical analysis, and classical expressions from the literature. Further, classical methods cannot provide the local field distributions in the composite, and it is demonstrated that, as the percolation threshold is approached, their predictions are increasingly unreliable.

1.0   Introduction

Physical phenomena such as heat conduction, diffusion, electric permittivity, magnetic permeability, and electric conductivity are governed by first-order tensor (vector) constitutive laws. These constitutive laws relate two field vectors via a second-order property tensor (e.g., Fourier's law of heat conduction). In composites, the constituent materials are governed by these vector laws, whereas the composite macroscopic behavior is governed by an effective constitutive law of the same form. There has been much effort targeted towards predicting the effective second-order property tensor of composite materials for the above physical phenomena. Expressions for composite effective thermal conductivities, based on various micromechanical analyses, have been derived, see for example Christensen (1979) and references cited there. Furthermore, expressions for the effective thermal conductivities of composites derived by Maxwell, Rayleigh, Bruggeman, as well as others, were recently summarized by Pietrak and Wisniewski (2015). Many other such expressions have been reported and applied in the literature, c.f. Hamilton and Crosser (1962), Springer and Tsai (1967), Kumar et al. (2011), Dinulovic and Rasua (2009), Avila et al. (2015). Likewise, the Mori-Tanaka (1973) method was employed by Hatta and Taya (1985) and Nan et al. (1997)

for the prediction of effective conductivities. These methods, however, while predicting effective properties, cannot provide the local field distributions. These local field distributions are important as they provide insight into the influence of microstructure on material performance (e.g., effective properties) and are a key factor in the design of fit-for-purpose materials consistent with an integrated computational materials engineering (ICME) paradigm. For example, local hot spots (e.g., temperature spikes) within a given material microstructure are likely zones of increased chemical or environmental reactivity and/or failure locations, thus suggesting the tailoring of the microstructure to minimize such spikes. As mentioned by Pietrak and Wisniewski (2015), expressions derived for any one of the physical phenomena governed by vector constitutive laws are applicable to the other types simply by substituting the correct composite constituent property types in the expressions, as shown in the next section. Finally, numerical methods have been extensively applied to composite micromechanics problems involving vector constitutive laws, c.f. Islam and Pramila (1999), Floury et al. (2008), Chmielewski and Wegelewski (2013).

Herein, the High-Fidelity Generalized Method of Cells (HFGMC) micromechanics theory (Aboudi et al., 2013) for periodic composite microstructures, is extended to model the aforementioned physical phenomena governed by vector constitutive laws. As shown in Aboudi et al. (2013), HFGMC is capable of predicting the effective mechanical properties of composites as well as the local field distributions that develop within the composite microstructure. For mechanical problems, the HFGMC has been extensively validated and applied for various continuous and discontinuous composite materials. Further, Haj-Ali et al. (2014) extended and applied HFGMC for modeling continuous piezoresistive composites.

For composites with continuous microstructures (those which have phase geometries that are constant in at least one direction) and orthotropic constituents, there exists a shear analogy enabling the calculation of the effective transverse property of the above vector constitutive laws from a mechanical analysis (Hashin, 1972). For example, the expression for the composite effective axial shear modulus is identical to that of the effective transverse thermal conductivity, provided the constituent shear moduli are replaced in this expression by the constituent transverse thermal conductivities. Clearly this analogy also applies to all physical phenomena governed by vector constitutive laws, e.g., diffusion, electric permittivity, etc. Given the fact that HFGMC predicts the effective axial shear moduli, this shear analogy can be readily applied for continuously reinforced composites. However, for the general case of composites that do not exhibit constant microstructural geometry in any direction (e.g., particulate, short fiber, and woven composites), as will be shown, the shear analogy is not valid. The present extension of HFGMC, which is independent of the shear analogy, enables the prediction of the full second-order effective property tensor (for the above family of vector constitutive laws) for arbitrary composite microstructures.

After first presenting the theoretical extension of the HFGMC, thermal conductivity and electric permittivity results are given for both continuous and discontinuous composites, including both effective properties and local fields for ordered and random composite microstructures. The HFGMC predictions are compared to measured values and numerical (finite element and boundary element) method results, exhibiting excellent agreement. In addition, comparisons are made to classical methods, such as Christensen's (1979) closed-form expression and the Mori-Tanaka method (through use of the shear analogy). The limitations of these classical methods are shown in the cases of complex microstructures and in the vicinity of the percolation threshold. Finally, the present HFGMC extension is applied to predict the effective properties and local field distributions for a woven composite microstructure for both the thermal and electric problems.

2.0 HFGMC Theory for Vector Constitutive Laws

Vector constitutive laws represent a wide range of technologically relevant physical phenomena. For example, the constitutive equation for heat conduction is given by Fourier's law,

$$\mathbf{q} = -\mathbf{\kappa} \nabla T \tag{1}$$

where $\mathbf{q}$ is the heat flux vector, $\mathbf{\kappa}$ is the second-order thermal conductivity tensor, and T is the temperature. The electrical permittivity constitutive equation is given by

$$\mathbf{D} = -\mathbf{\epsilon} \nabla \phi \tag{2}$$

where $\mathbf{D}$ is the electrical displacement vector, $\mathbf{\epsilon}$ is the second-order electric permittivity tensor, and ϕ is the electric potential such that the electric field vector is given by $\mathbf{E} = -\nabla \phi$. Similarly, the magnetic permeability constitutive equation is given by

$$\mathbf{B} = -\mathbf{\mu} \nabla \xi \tag{3}$$

where $\mathbf{B}$ is the magnetic flux density vector, $\mathbf{\mu}$ is the second-order magnetic permeability tensor, and ξ is the magnetic potential such that the magnetic field vector is given by $\mathbf{H} = -\nabla \xi$. The electrical conduction constitutive equation is given by

$$\mathbf{J} = -\mathbf{\sigma} \nabla \phi \tag{4}$$

where $\mathbf{J}$ is the electric current density vector, and $\mathbf{\sigma}$ is the second-order electric conductivity tensor. The constitutive equation for diffusion is given by Fick's law,

$$\mathbf{j} = -\mathbf{d} \nabla C \tag{5}$$

where $\mathbf{j}$ is the permeate flux vector, $\mathbf{d}$ is the second-order diffusivity tensor, and C is concentration. All five of these constitutive laws (as well as others such as Darcy's law for fluid flow through a porous medium) can be written in the following general form

$$\mathbf{Y} = -\mathbf{Z} \nabla \psi = \mathbf{Z} \mathbf{X} \tag{6}$$

where $\mathbf{Y}$ denotes any of $\mathbf{q}$, $\mathbf{D}$, $\mathbf{B}$, $\mathbf{J}$, or $\mathbf{j}$, ψ denotes any of T, ϕ, ξ, or C, and $\mathbf{X}$ denotes any of $-\nabla T$, $-\mathbf{E}$, $-\mathbf{H}$, or $-\nabla C$. The governing equation for all of these physical phenomena is given by,

$$\nabla \cdot \mathbf{Y} = 0 \tag{7}$$

The HFGMC micromechanical model is employed herein to predict the effective properties, $\mathbf{Z}$, of composites with various microstructures. The mechanical form of this theory has been fully described by Aboudi et al. (2013). The triply periodic HFGMC, with a vector constitutive law given by Equation (6), is outlined in the following. The triply periodic microstructure considered is shown in Figure 1 (a) in terms of the global coordinates (x_1, x_2, x_3). The repeating unit cell (RUC), Figure 1 (b), defined with respect to local coordinates (y_1, y_2, y_3), of such a composite is divided into N_α by N_β by N_γ subcells in the y_1, y_2, and y_3 directions, respectively. Each subcell is identified by the indices $(\alpha\beta\gamma)$ with $\alpha = 1, \ldots, N_\alpha$, $\beta = 1, \ldots, N_\beta$, and $\gamma = 1, \ldots, N_\gamma$, and may contain a distinct homogeneous material. The dimensions of subcell $(\alpha\beta\gamma)$ in the y_1,

y_2, and y_3 directions are denoted by d_α, h_β, and l_γ, respectively. A local coordinate system ($\bar{y}_1^{(\alpha)}, \bar{y}_2^{(\beta)}, \bar{y}_3^{(\gamma)}$) is introduced in each subcell whose origin is located at its center. The local (subcell) vector constitutive equation of the anisotropic material is given by,

$$\mathbf{Y}^{(\alpha\beta\gamma)} = \mathbf{Z}^{(\alpha\beta\gamma)} \mathbf{X}^{(\alpha\beta\gamma)} \tag{8}$$

The HFGMC theory is based on a second-order expansion of the scalar variable $\psi^{(\alpha\beta\gamma)}$ (which represents temperature, potential, or concentration; henceforth referred to as potential) in the subcell ($\alpha\beta\gamma$) as follows

$$\psi^{(\alpha\beta\gamma)} = \bar{X}_j x_j + \theta_{(000)}^{(\alpha\beta\gamma)} + \bar{y}_1^{(\alpha)}\theta_{(100)}^{(\alpha\beta\gamma)} + \bar{y}_2^{(\beta)}\theta_{(010)}^{(\alpha\beta\gamma)} + \bar{y}_3^{(\gamma)}\theta_{(001)}^{(\alpha\beta\gamma)}$$
$$+ \frac{1}{2}\left(3\bar{y}_1^{(\alpha)2} - \frac{d_\alpha^2}{4}\right)\theta_{(200)}^{(\alpha\beta\gamma)} + \frac{1}{2}\left(3\bar{y}_2^{(\beta)2} - \frac{h_\beta^2}{4}\right)\theta_{(020)}^{(\alpha\beta\gamma)} + \frac{1}{2}\left(3\bar{y}_3^{(\gamma)2} - \frac{l_\gamma^2}{4}\right)\theta_{(002)}^{(\alpha\beta\gamma)} \tag{9}$$
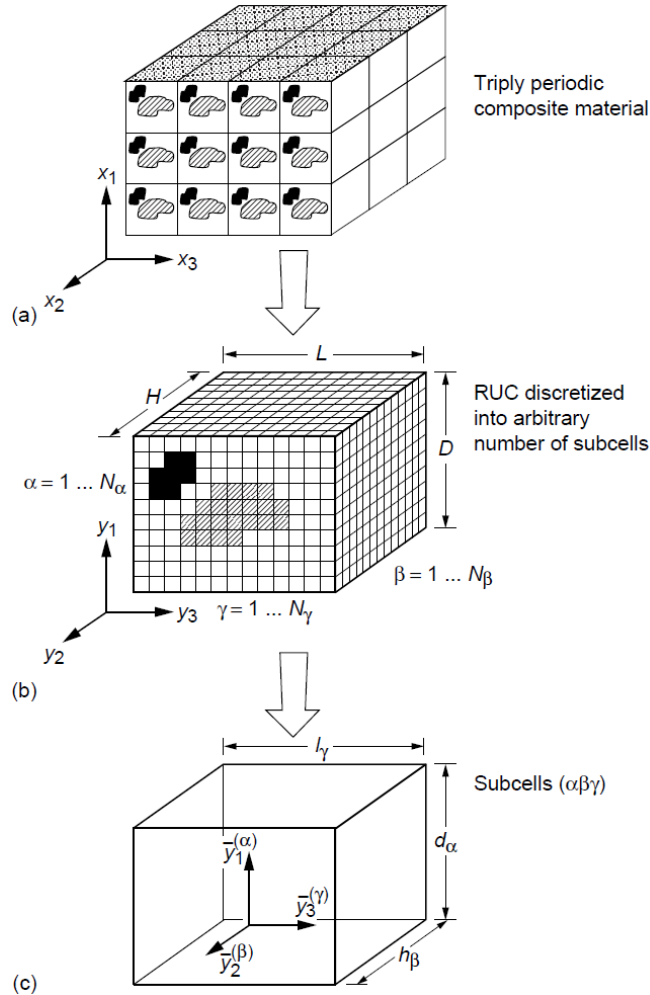

Figure 1.—(a) A multiphase composite with triply-periodic microstructures defined with respect to global coordinates (x_1, x_2, x_3). (b) The repeating unit cell (RUC) is represented with respect to local coordinates (y_1, y_2, y_3). It is divided into N_α by N_β by N_γ subcells, in the y_1, y_2, and y_3 directions, respectively. (c) A characteristic subcell ($\alpha\beta\gamma$) with local coordinates ($\bar{y}_1^{(\alpha)}, \bar{y}_2^{(\beta)}, \bar{y}_3^{(\gamma)}$) whose origin is located at its center.

where $\overline{X}_j$ are the components of the global (far-field) potential gradient vector, $\overline{\mathbf{X}}$, $\theta_{(000)}^{(\alpha\beta\gamma)}$ is the volume-averaged potential of subcell $(\alpha\beta\gamma)$, and the higher-order terms $\theta_{(lmn)}^{(\alpha\beta\gamma)}$ must be determined by implementing the interfacial and periodic conditions.

The following field quantities are defined

$$Q_{i(lmn)}^{(\alpha\beta\gamma)} = \frac{1}{d_\alpha h_\beta l_\gamma} \int_{-d_\alpha/2}^{d_\alpha/2} \int_{-h_\beta/2}^{h_\beta/2} \int_{-l_\gamma/2}^{l_\gamma/2} Y_i^{(\alpha\beta\gamma)} \left(\overline{y}_1^{(\alpha)}\right)^l \left(\overline{y}_2^{(\beta)}\right)^m \left(\overline{y}_3^{(\gamma)}\right)^n d\overline{y}_1^{(\alpha)} \, d\overline{y}_2^{(\beta)} \, d\overline{y}_3^{(\gamma)} \tag{10}$$

It follows that

$$Q_{i(000)}^{(\alpha\beta\gamma)} = Z_{i1}^{(\alpha\beta\gamma)}\left(\theta_{(100)}^{(\alpha\beta\gamma)} + \overline{X}_1\right) + Z_{i2}^{(\alpha\beta\gamma)}\left(\theta_{(010)}^{(\alpha\beta\gamma)} + \overline{X}_2\right) + Z_{i3}^{(\alpha\beta\gamma)}\left(\theta_{(001)}^{(\alpha\beta\gamma)} + \overline{X}_3\right) \quad i = 1,2,3 \tag{11}$$

In addition,

$$Q_{i(100)}^{(\alpha\beta\gamma)} = \frac{d_\alpha^2}{4} Z_{i1}^{(\alpha\beta\gamma)} \theta_{(200)}^{(\alpha\beta\gamma)} \quad i = 1,2,3 \tag{12}$$

$$Q_{i(010)}^{(\alpha\beta\gamma)} = \frac{h_\beta^2}{4} Z_{i2}^{(\alpha\beta\gamma)} \theta_{(020)}^{(\alpha\beta\gamma)} \quad i = 1,2,3 \tag{13}$$

$$Q_{i(001)}^{(\alpha\beta\gamma)} = \frac{l_\gamma^2}{4} Z_{i3}^{(\alpha\beta\gamma)} \theta_{(002)}^{(\alpha\beta\gamma)} \quad i = 1,2,3 \tag{14}$$

The governing equation (7) takes the form

$$\frac{1}{d_\alpha^2} Q_{1(100)}^{(\alpha\beta\gamma)} + \frac{1}{h_\beta^2} Q_{2(010)}^{(\alpha\beta\gamma)} + \frac{1}{l_\gamma^2} Q_{3(001)}^{(\alpha\beta\gamma)} = 0 \tag{15}$$

The surface-averaged values of $Y_i^{(\alpha\beta\gamma)}$ are given by

$$\chi_1^{\pm(\alpha\beta\gamma)} = \frac{1}{h_\beta l_\gamma} \int_{-h_\beta/2}^{h_\beta/2} \int_{-l_\gamma/2}^{l_\gamma/2} Y_1^{(\alpha\beta\gamma)}\left(\overline{y}_1^{(\alpha)} = \pm\frac{d_\alpha}{2}\right) d\overline{y}_2^{(\beta)} d\overline{y}_3^{(\gamma)} \tag{16}$$

$$\chi_2^{\pm(\alpha\beta\gamma)} = \frac{1}{d_\alpha l_\gamma} \int_{-d_\alpha/2}^{d_\alpha/2} \int_{-l_\gamma/2}^{l_\gamma/2} Y_2^{(\alpha\beta\gamma)}\left(\overline{y}_2^{(\beta)} = \pm\frac{h_\beta}{2}\right) d\overline{y}_1^{(\alpha)} d\overline{y}_3^{(\gamma)} \tag{17}$$

$$\chi_3^{\pm(\alpha\beta\gamma)} = \frac{1}{d_\alpha h_\beta} \int_{-d_\alpha/2}^{d_\alpha/2} \int_{-h_\beta/2}^{h_\beta/2} Y_3^{(\alpha\beta\gamma)}\left(\overline{y}_3^{(\gamma)} = \pm\frac{l_\gamma}{2}\right) d\overline{y}_1^{(\alpha)} d\overline{y}_2^{(\beta)} \tag{18}$$

Using these surface-averaged values reduces Equation (15) to

$$\frac{1}{d_\alpha}\left(\chi_1^{+(\alpha\beta\gamma)} - \chi_1^{-(\alpha\beta\gamma)}\right) + \frac{1}{h_\beta}\left(\chi_2^{+(\alpha\beta\gamma)} - \chi_2^{-(\alpha\beta\gamma)}\right) + \frac{1}{l_\gamma}\left(\chi_3^{+(\alpha\beta\gamma)} - \chi_3^{-(\alpha\beta\gamma)}\right) = 0 \tag{19}$$

The surface-averaged potential quantities can be defined as

$$\omega_1^{\pm(\alpha\beta\gamma)} = \frac{1}{h_\beta l_\gamma} \int_{-h_\beta/2}^{h_\beta/2} \int_{-l_\gamma/2}^{l_\gamma/2} \psi^{(\alpha\beta\gamma)}\left(\bar{y}_1^{(\alpha)} = \pm\frac{d_\alpha}{2}\right) d\bar{y}_2^{(\beta)} d\bar{y}_3^{(\gamma)} \tag{20}$$

$$\omega_2^{\pm(\alpha\beta\gamma)} = \frac{1}{d_\alpha l_\gamma} \int_{-d_\alpha/2}^{d_\alpha/2} \int_{-l_\gamma/2}^{l_\gamma/2} \psi^{(\alpha\beta\gamma)}\left(\bar{y}_2^{(\beta)} = \pm\frac{h_\beta}{2}\right) d\bar{y}_1^{(\alpha)} d\bar{y}_3^{(\gamma)} \tag{21}$$

$$\omega_3^{\pm(\alpha\beta\gamma)} = \frac{1}{d_\alpha h_\beta} \int_{-d_\alpha/2}^{d_\alpha/2} \int_{-h_\beta/2}^{h_\beta/2} \psi^{(\alpha\beta\gamma)}\left(\bar{y}_3^{(\gamma)} = \pm\frac{l_\gamma}{2}\right) d\bar{y}_1^{(\alpha)} d\bar{y}_2^{(\beta)} \tag{22}$$

By employing the potential expansion, Equation (9),

$$\begin{aligned}
\omega_1^{\pm(\alpha\beta\gamma)} &= \theta_{(000)}^{(\alpha\beta\gamma)} \pm \frac{d_\alpha}{2}\theta_{(100)}^{(\alpha\beta\gamma)} + \frac{d_\alpha^2}{4}\theta_{(200)}^{(\alpha\beta\gamma)} \\
\omega_2^{\pm(\alpha\beta\gamma)} &= \theta_{(000)}^{(\alpha\beta\gamma)} \pm \frac{h_\beta}{2}\theta_{(010)}^{(\alpha\beta\gamma)} + \frac{h_\beta^2}{4}\theta_{(020)}^{(\alpha\beta\gamma)} \\
\omega_3^{\pm(\alpha\beta\gamma)} &= \theta_{(000)}^{(\alpha\beta\gamma)} \pm \frac{l_\gamma}{2}\theta_{(001)}^{(\alpha\beta\gamma)} + \frac{l_\gamma^2}{4}\theta_{(002)}^{(\alpha\beta\gamma)}
\end{aligned} \tag{23}$$

By subtracting $\omega_i^{-(\alpha\beta\gamma)}$ from $\omega_i^{+(\alpha\beta\gamma)}$, one obtains

$$\theta_{(100)}^{(\alpha\beta\gamma)} = \frac{1}{d_\alpha}\left(\omega_1^{+(\alpha\beta\gamma)} - \omega_1^{-(\alpha\beta\gamma)}\right) \tag{24}$$

$$\theta_{(010)}^{(\alpha\beta\gamma)} = \frac{1}{h_\beta}\left(\omega_2^{+(\alpha\beta\gamma)} - \omega_2^{-(\alpha\beta\gamma)}\right) \tag{25}$$

$$\theta_{(001)}^{(\alpha\beta\gamma)} = \frac{1}{l_\gamma}\left(\omega_3^{+(\alpha\beta\gamma)} - \omega_3^{-(\alpha\beta\gamma)}\right) \tag{26}$$

Adding $\omega_i^{-(\alpha\beta\gamma)}$ to $\omega_i^{+(\alpha\beta\gamma)}$ yields

$$\theta_{(200)}^{(\alpha\beta\gamma)} = \frac{2}{d_\alpha^2}\left(\omega_1^{+(\alpha\beta\gamma)} + \omega_1^{-(\alpha\beta\gamma)}\right) - \frac{4}{d_\alpha^2}\theta_{(000)}^{(\alpha\beta\gamma)} \tag{27}$$

$$\theta_{(020)}^{(\alpha\beta\gamma)} = \frac{2}{h_\beta^2}\left(\omega_2^{+(\alpha\beta\gamma)} + \omega_2^{-(\alpha\beta\gamma)}\right) - \frac{4}{h_\beta^2}\theta_{(000)}^{(\alpha\beta\gamma)} \tag{28}$$

$$\theta_{(002)}^{(\alpha\beta\gamma)} = \frac{2}{l_\gamma^2}\left(\omega_3^{+(\alpha\beta\gamma)} + \omega_3^{-(\alpha\beta\gamma)}\right) - \frac{4}{l_\gamma^2}\theta_{(000)}^{(\alpha\beta\gamma)} \tag{29}$$

It remains, therefore, to establish $\theta_{(000)}^{(\alpha\beta\gamma)}$ in terms of $\omega_i^{\pm(\alpha\beta\gamma)}$. This is achieved by employing the governing equation. To this end, substituting Equations (12) to (14) into Equation (15) yields

$$Z_{11}^{(\alpha\beta\gamma)}\theta_{(200)}^{(\alpha\beta\gamma)} + Z_{22}^{(\alpha\beta\gamma)}\theta_{(020)}^{(\alpha\beta\gamma)} + Z_{33}^{(\alpha\beta\gamma)}\theta_{(002)}^{(\alpha\beta\gamma)} = 0 \tag{30}$$

Using Equations (27) to (29) in Equation (30), and solving for $\theta_{(000)}^{(\alpha\beta\gamma)}$, the following expression is obtained

$$\theta_{(000)}^{(\alpha\beta\gamma)} = P_1^{(\alpha\beta\gamma)}\left(\omega_1^{+(\alpha\beta\gamma)} + \omega_1^{-(\alpha\beta\gamma)}\right) + P_2^{(\alpha\beta\gamma)}\left(\omega_2^{+(\alpha\beta\gamma)} + \omega_2^{-(\alpha\beta\gamma)}\right) + P_3^{(\alpha\beta\gamma)}\left(\omega_3^{+(\alpha\beta\gamma)} + \omega_3^{-(\alpha\beta\gamma)}\right) \tag{31}$$

where

$$P_1^{(\alpha\beta\gamma)} = \frac{Z_{11}^{(\alpha\beta\gamma)}}{d_\alpha^2}\left(\frac{2}{d_\alpha^2}Z_{11}^{(\alpha\beta\gamma)} + \frac{2}{h_\beta^2}Z_{22}^{(\alpha\beta\gamma)} + \frac{2}{l_\gamma^2}Z_{33}^{(\alpha\beta\gamma)}\right)^{-1} \tag{32}$$

$$P_2^{(\alpha\beta\gamma)} = \frac{Z_{22}^{(\alpha\beta\gamma)}}{h_\beta^2}\left(\frac{2}{d_\alpha^2}Z_{11}^{(\alpha\beta\gamma)} + \frac{2}{h_\beta^2}Z_{22}^{(\alpha\beta\gamma)} + \frac{2}{l_\gamma^2}Z_{33}^{(\alpha\beta\gamma)}\right)^{-1} \tag{33}$$

$$P_3^{(\alpha\beta\gamma)} = \frac{Z_{33}^{(\alpha\beta\gamma)}}{l_\gamma^2}\left(\frac{2}{d_\alpha^2}Z_{11}^{(\alpha\beta\gamma)} + \frac{2}{h_\beta^2}Z_{22}^{(\alpha\beta\gamma)} + \frac{2}{l_\gamma^2}Z_{33}^{(\alpha\beta\gamma)}\right)^{-1} \tag{34}$$

Consequently, using Equation (31) in Equations (27) to (29), the following expressions can be obtained

$$\theta_{(200)}^{(\alpha\beta\gamma)} = F_1^{(\alpha\beta\gamma)}\left(\omega_1^{+(\alpha\beta\gamma)} + \omega_1^{-(\alpha\beta\gamma)}\right) + F_2^{(\alpha\beta\gamma)}\left(\omega_2^{+(\alpha\beta\gamma)} + \omega_2^{-(\alpha\beta\gamma)}\right) + F_3^{(\alpha\beta\gamma)}\left(\omega_3^{+(\alpha\beta\gamma)} + \omega_3^{-(\alpha\beta\gamma)}\right) \tag{35}$$

$$\theta_{(020)}^{(\alpha\beta\gamma)} = G_1^{(\alpha\beta\gamma)}\left(\omega_1^{+(\alpha\beta\gamma)} + \omega_1^{-(\alpha\beta\gamma)}\right) + G_2^{(\alpha\beta\gamma)}\left(\omega_2^{+(\alpha\beta\gamma)} + \omega_2^{-(\alpha\beta\gamma)}\right) + G_3^{(\alpha\beta\gamma)}\left(\omega_3^{+(\alpha\beta\gamma)} + \omega_3^{-(\alpha\beta\gamma)}\right) \quad (36)$$

$$\theta_{(002)}^{(\alpha\beta\gamma)} = H_1^{(\alpha\beta\gamma)}\left(\omega_1^{+(\alpha\beta\gamma)} + \omega_1^{-(\alpha\beta\gamma)}\right) + H_2^{(\alpha\beta\gamma)}\left(\omega_2^{+(\alpha\beta\gamma)} + \omega_2^{-(\alpha\beta\gamma)}\right) + H_3^{(\alpha\beta\gamma)}\left(\omega_3^{+(\alpha\beta\gamma)} + \omega_3^{-(\alpha\beta\gamma)}\right) \quad (37)$$

where

$$F_1^{(\alpha\beta\gamma)} = \frac{2}{d_\alpha^2} - \frac{4}{d_\alpha^2}P_1^{(\alpha\beta\gamma)}, \quad F_2^{(\alpha\beta\gamma)} = -\frac{4}{d_\alpha^2}P_2^{(\alpha\beta\gamma)}, \quad F_3^{(\alpha\beta\gamma)} = -\frac{4}{d_\alpha^2}P_3^{(\alpha\beta\gamma)} \quad (38)$$

$$G_1^{(\alpha\beta\gamma)} = -\frac{4}{h_\beta^2}P_1^{(\alpha\beta\gamma)}, \quad G_2^{(\alpha\beta\gamma)} = \frac{2}{h_\beta^2} - \frac{4}{h_\beta^2}P_2^{(\alpha\beta\gamma)}, \quad G_3^{(\alpha\beta\gamma)} = -\frac{4}{h_\beta^2}P_3^{(\alpha\beta\gamma)} \quad (39)$$

$$H_1^{(\alpha\beta\gamma)} = -\frac{4}{l_\gamma^2}P_1^{(\alpha\beta\gamma)}, \quad H_2^{(\alpha\beta\gamma)} = -\frac{4}{l_\gamma^2}P_2^{(\alpha\beta\gamma)}, \quad H_3^{(\alpha\beta\gamma)} = \frac{2}{l_\gamma^2} - \frac{4}{l_\gamma^2}P_3^{(\alpha\beta\gamma)} \quad (40)$$

Using the potential expansion, Equation (9), in Equations (16) to (18), in conjunction with $X = -\nabla\psi$, one obtains

$$\chi_1^{\pm(\alpha\beta\gamma)} = -Z_{11}^{(\alpha\beta\gamma)}\left[\overline{X}_1 + \theta_{(100)}^{(\alpha\beta\gamma)} \pm \frac{3d_\alpha}{2}\theta_{(200)}^{(\alpha\beta\gamma)}\right] - Z_{12}^{(\alpha\beta\gamma)}\theta_{(010)}^{(\alpha\beta\gamma)} - Z_{13}^{(\alpha\beta\gamma)}\theta_{(001)}^{(\alpha\beta\gamma)} \quad (41)$$

$$\chi_2^{\pm(\alpha\beta\gamma)} = -Z_{21}^{(\alpha\beta\gamma)}\theta_{(100)}^{(\alpha\beta\gamma)} - Z_{22}^{(\alpha\beta\gamma)}\left[\overline{X}_2 + \theta_{(010)}^{(\alpha\beta\gamma)} \pm \frac{3h_\beta}{2}\theta_{(020)}^{(\alpha\beta\gamma)}\right] - Z_{23}^{(\alpha\beta\gamma)}\theta_{(001)}^{(\alpha\beta\gamma)} \quad (42)$$

$$\chi_2^{\pm(\alpha\beta\gamma)} = -Z_{31}^{(\alpha\beta\gamma)}\theta_{(100)}^{(\alpha\beta\gamma)} - Z_{32}^{(\alpha\beta\gamma)}\theta_{(010)}^{(\alpha\beta\gamma)} - Z_{33}^{(\alpha\beta\gamma)}\left[\overline{X}_3 + \theta_{(001)}^{(\alpha\beta\gamma)} \pm \frac{3l_\gamma}{2}\theta_{(002)}^{(\alpha\beta\gamma)}\right] \quad (43)$$

Using Equations (24) to (29) in Equations (41) to (43), one obtains the following expressions

$$\chi_1^{\pm(\alpha\beta\gamma)} = -Z_{11}^{(\alpha\beta\gamma)}\left\{\overline{X}_1 + \frac{1}{d_\alpha}\left(\omega_1^{+(\alpha\beta\gamma)} - \omega_1^{-(\alpha\beta\gamma)}\right)\right.$$

$$\left. \pm \frac{3d_\alpha}{2}\left[F_1^{(\alpha\beta\gamma)}\left(\omega_1^{+(\alpha\beta\gamma)} + \omega_1^{-(\alpha\beta\gamma)}\right) + F_2^{(\alpha\beta\gamma)}\left(\omega_2^{+(\alpha\beta\gamma)} + \omega_2^{-(\alpha\beta\gamma)}\right) + F_3^{(\alpha\beta\gamma)}\left(\omega_3^{+(\alpha\beta\gamma)} + \omega_3^{-(\alpha\beta\gamma)}\right)\right]\right\} \quad (44)$$

$$- \frac{Z_{12}^{(\alpha\beta\gamma)}}{h_\beta}\left(\omega_2^{+(\alpha\beta\gamma)} - \omega_2^{-(\alpha\beta\gamma)}\right) - \frac{Z_{13}^{(\alpha\beta\gamma)}}{l_\gamma}\left(\omega_3^{+(\alpha\beta\gamma)} - \omega_3^{-(\alpha\beta\gamma)}\right)$$

$$
\chi_2^{\pm(\alpha\beta\gamma)} = -\frac{Z_{21}^{(\alpha\beta\gamma)}}{d_\alpha}\left(\omega_1^{+(\alpha\beta\gamma)} - \omega_1^{-(\alpha\beta\gamma)}\right) - Z_{22}^{(\alpha\beta\gamma)}\left\{\overline{X}_2 + \frac{1}{h_\beta}\left(\omega_2^{+(\alpha\beta\gamma)} - \omega_2^{-(\alpha\beta\gamma)}\right)\right.
$$
$$
\left. \pm \frac{3h_\beta}{2}\left[G_1^{(\alpha\beta\gamma)}\left(\omega_1^{+(\alpha\beta\gamma)} + \omega_1^{-(\alpha\beta\gamma)}\right) + G_2^{(\alpha\beta\gamma)}\left(\omega_2^{+(\alpha\beta\gamma)} + \omega_2^{-(\alpha\beta\gamma)}\right) + G_3^{(\alpha\beta\gamma)}\left(\omega_3^{+(\alpha\beta\gamma)} + \omega_3^{-(\alpha\beta\gamma)}\right)\right]\right\} \quad (45)
$$
$$
- \frac{Z_{23}^{(\alpha\beta\gamma)}}{l_\gamma}\left(\omega_3^{+(\alpha\beta\gamma)} - \omega_3^{-(\alpha\beta\gamma)}\right)
$$

$$
\chi_3^{\pm(\alpha\beta\gamma)} = -\frac{Z_{31}^{(\alpha\beta\gamma)}}{d_\alpha}\left(\omega_1^{+(\alpha\beta\gamma)} - \omega_1^{-(\alpha\beta\gamma)}\right) - \frac{Z_{32}^{(\alpha\beta\gamma)}}{h_\beta}\left(\omega_2^{+(\alpha\beta\gamma)} - \omega_2^{-(\alpha\beta\gamma)}\right) - Z_{33}^{(\alpha\beta\gamma)}\left\{\overline{X}_3 + \frac{1}{l_\gamma}\left(\omega_3^{+(\alpha\beta\gamma)} - \omega_3^{-(\alpha\beta\gamma)}\right)\right.
$$
$$
(46)
$$
$$
\left. \pm \frac{3l_\gamma}{2}\left[H_1^{(\alpha\beta\gamma)}\left(\omega_1^{+(\alpha\beta\gamma)} + \omega_1^{-(\alpha\beta\gamma)}\right) + H_2^{(\alpha\beta\gamma)}\left(\omega_2^{+(\alpha\beta\gamma)} + \omega_2^{-(\alpha\beta\gamma)}\right) + H_3^{(\alpha\beta\gamma)}\left(\omega_3^{+(\alpha\beta\gamma)} + \omega_3^{-(\alpha\beta\gamma)}\right)\right]\right\}
$$

Equations (44) to (46) can be written in compact form as

$$
\begin{Bmatrix} \chi_1^+ \\ \chi_1^- \\ \chi_2^+ \\ \chi_2^- \\ \chi_3^+ \\ \chi_3^- \end{Bmatrix}^{(\alpha\beta\gamma)} = [\mathbf{k}]^{(\alpha\beta\gamma)} \begin{Bmatrix} \omega_1^+ \\ \omega_1^- \\ \omega_2^+ \\ \omega_2^- \\ \omega_3^+ \\ \omega_3^- \end{Bmatrix}^{(\alpha\beta\gamma)} - \begin{Bmatrix} Z_{11}\overline{X}_1 \\ Z_{11}\overline{X}_1 \\ Z_{22}\overline{X}_2 \\ Z_{22}\overline{X}_2 \\ Z_{33}\overline{X}_3 \\ Z_{33}\overline{X}_3 \end{Bmatrix}^{(\alpha\beta\gamma)} \quad (47)
$$

where $[\mathbf{k}]^{(\alpha\beta\gamma)}$ is a 6×6 matrix whose elements depend on the dimensions of the subcell ($\alpha\beta\gamma$) and the properties of the material filling the subcell.

In the presence of perfect bonding between the constituents, the surface-averaged potential quantities between neighboring subcells are continuous,

$$
\omega_1^{+(\alpha,\beta,\gamma)} = \omega_1^{-(\alpha+1,\beta,\gamma)}
$$
$$
\omega_2^{+(\alpha,\beta,\gamma)} = \omega_2^{-(\alpha,\beta+1,\gamma)} \quad (48)
$$
$$
\omega_3^{+(\alpha,\beta,\gamma)} = \omega_3^{-(\alpha,\beta,\gamma+1)}
$$

In addition, interfacial continuity of the surface-averaged $Y_i^{(\alpha\beta\gamma)}$ quantities, denoted by $\chi_i^{(\alpha\beta\gamma)}$, is expressed as

$$
\chi_1^{+(\alpha,\beta,\gamma)} = \chi_1^{-(\alpha+1,\beta,\gamma)}
$$
$$
\chi_2^{+(\alpha,\beta,\gamma)} = \chi_2^{-(\alpha,\beta+1,\gamma)} \quad (49)
$$
$$
\chi_3^{+(\alpha,\beta,\gamma)} = \chi_3^{-(\alpha,\beta,\gamma+1)}
$$

Finally, the periodicity conditions, which require that the surface-averaged quantities are identical on the opposite sides of the RUC, are given by

$$\omega_1^{+(N_\alpha\beta\gamma)} = \omega_1^{-(1\beta\gamma)}$$

$$\omega_2^{+(\alpha N_\beta\gamma)} = \omega_2^{-(\alpha 1\gamma)} \tag{50}$$

$$\omega_3^{+(\alpha\beta N_\gamma)} = \omega_3^{-(\alpha\beta 1)}$$

$$\chi_1^{+(N_\alpha\beta\gamma)} = \chi_1^{-(1\beta\gamma)}$$

$$\chi_2^{+(\alpha N_\beta\gamma)} = \chi_2^{-(\alpha 1\gamma)} \tag{51}$$

$$\chi_3^{+(\alpha\beta N_\gamma)} = \chi_3^{-(\alpha\beta 1)}$$

Equation (47) shows that for each subcell $(\alpha\beta\gamma)$ there are 6 unknown surface-averaged potential quantities $\omega_i^{\pm(\alpha\beta\gamma)}$ that need to be determined. For a RUC with $\alpha=1,2,\ldots,N_\alpha$, $\beta = 1,2,\ldots,N_\beta$, and $\gamma = 1,2,\ldots,N_\gamma$, there are $N_\alpha N_\beta N_\gamma$ subcells. Thus the number of unknown surface-averaged potential quantities $\omega_i^{\pm(\alpha\beta\gamma)}$ is $6N_\alpha N_\beta N_\gamma$. On the other hand, there are a total of $(N_\alpha - 1)N_\beta N_\gamma + (N_\beta - 1)N_\alpha N_\gamma + (N_\gamma - 1)N_\alpha N_\beta$ internal subcell interfaces on which the continuity of the surface-averaged quantities, $\omega_i^{(\alpha\beta\gamma)}$ and $\chi_i^{(\alpha\beta\gamma)}$, provides $2[(N_\alpha - 1)N_\beta N_\gamma + (N_\beta - 1)N_\alpha N_\gamma + (N_\gamma - 1)N_\alpha N_\beta]$ equations. In addition, the periodicity conditions provide $2[N_\beta N_\gamma + N_\alpha N_\gamma + N_\alpha N_\beta]$ equations. Thus the total number of equations is exactly equal to the number of unknowns, $6N_\beta N_\gamma$.

The full system of $6N_\alpha N_\beta N_\gamma$ equations can be assembled from Equations (47) to (51) and expressed as

$$\mathbf{K}\,\mathbf{\Omega} = \mathbf{f} \tag{52}$$

where $\mathbf{K}$ contains information on the geometry of the subcells and material properties, $\mathbf{\Omega}$ is the vector of unknown surface-averaged potentials, and $\mathbf{f}$ contains the far field loading and material properties. The solution of this system of linear algebraic equations enables establishment of the following relations, which connect the local fields in the subcells to the applied far field as follows

$$\mathbf{X}^{(\alpha\beta\gamma)} = \mathbf{A}^{(\alpha\beta\gamma)}\,\overline{\mathbf{X}} \tag{53}$$

where $\mathbf{A}^{(\alpha\beta\gamma)}$ is the concentration tensor for subcell $(\alpha\beta\gamma)$.

Volume-averaging $\mathbf{Y}^{(\alpha\beta\gamma)}$ over the entire RUC provides

$$\overline{\mathbf{Y}} = \frac{1}{DHL}\sum_{\alpha=1}^{N_\alpha}\sum_{\beta=1}^{N_\beta}\sum_{\gamma=1}^{N_\gamma} d_\alpha h_\beta l_\gamma \mathbf{Y}^{(\alpha\beta\gamma)} \tag{54}$$

where D, H, and L are the overall dimensions of the RUC, see **Error! Reference source not found.**(b). Using the subcell constitutive Equation (8), along with Equations (53) and (54), one obtains the global (effective) constitutive equation for the composite

$$\overline{\mathbf{Y}} = \mathbf{Z}^* \overline{\mathbf{X}} \tag{55}$$

where $\mathbf{Z}^*$ is the effective property tensor of the composite, which is given by

$$\mathbf{Z}^* = \frac{1}{DHL} \sum_{\alpha=1}^{N_\alpha} \sum_{\beta=1}^{N_\beta} \sum_{\gamma=1}^{N_\gamma} d_\alpha h_\beta l_\gamma \, \mathbf{Z}^{(\alpha\beta\gamma)} \mathbf{A}^{(\alpha\beta\gamma)} \tag{56}$$

In conclusion, the present HFGMC theory provides the homogenized macroscopic vector constitutive Equation (55), which established the overall behavior of the composite whose constituents are governed by any vector constitutive law, such as those given by Equations (1) to (5). It should be emphasized that HFGMC also provides the local field distributions within the RUC from Equations (53) and (8).

3.0 Results and Discussion

Predictions from the above general HFGMC micromechanics theory are presented below for an array of ordered and disordered, continuous and discontinuous, composite microstructures for both the heat conduction problem and the electric permittivity problem. Both effective properties and detailed local fields are shown with the results divided into five subsections. Comparisons are made to experimental and numerical model results from the literature, along with classical methods such as Christensen's (1979) expressions for the effective transverse thermal conductivity of composites (based on spherical and cylindrical inclusion models) and the Mori-Tanaka method (1973) through the use of the "shear analogy" (Hashin, 1972), as discussed below. Note that, for the continuous composite cases, attention has been focused on the transverse properties, as the effective property calculation in the axial (continuous) direction is trivial since it obeys the Voigt (rule of mixtures) approximation.

By replacing the constituent shear moduli with the constituent transverse thermal conductivity in an expression for the effective axial shear modulus of a continuously reinforced composite, the effective transverse thermal conductivity can be calculated. This "shear analogy" (see Hashin, 1972) is not valid for discontinuous composites because, in the mechanical problem, which is the basis of the analogy, all displacement components vary in all directions. To clarify this point, consider a composite in which the axial direction is x_1. The axial shear stresses are given by,

$$\sigma_{12} = G_{12}\left(\frac{\partial u_1}{\partial x_2} + \frac{\partial u_2}{\partial x_1}\right), \qquad \sigma_{13} = G_{13}\left(\frac{\partial u_1}{\partial x_3} + \frac{\partial u_3}{\partial x_1}\right) \tag{1}$$

In the shear analogy, σ_{12} and σ_{13} correspond to the heat flux components q_2 and q_3, respectively, whereas the shear moduli, G_{12} and G_{13}, correspond to the transverse thermal conductivity components, $-\kappa_2$ and $-\kappa_3$, respectively. In order for the analogy to be valid, u_1 must correspond to the temperature T, so that,

$$q_2 = -\kappa_{22}\frac{\partial T}{\partial x_2}, \qquad q_3 = -\kappa_{33}\frac{\partial T}{\partial x_3} \tag{2}$$

Consequently, this requires that $\partial u_2/\partial x_1 = \partial u_3/\partial x_1 = 0$, which is the case in continuously reinforced composites. For discontinuously reinforced composites, on the other hand, these gradients are in general non-zero, so the shear analogy is not valid. As for the governing equations, in the mechanical problem, the first equation of equilibrium is

$$\frac{\partial \sigma_{11}}{\partial x_1} + \frac{\partial \sigma_{12}}{\partial x_2} + \frac{\partial \sigma_{13}}{\partial x_3} = 0 \tag{3}$$

whereas, the heat equation is given by

$$\frac{\partial q_1}{\partial x_1} + \frac{\partial q_2}{\partial x_2} + \frac{\partial q_3}{\partial x_3} = 0 \tag{4}$$

Here too, these equations are identical (given the above correspondences) provided that $\partial/\partial x_1 = 0$.

3.1 Thermal Conductivity of a Composite With Varying Constituent Property Contrast Ratio

The effective thermal conductivity predictions of HFGMC have been compared to finite element results presented by Tang and Yu (2007) for a continuous unidirectional composite whose isotropic constituent's thermal conductivity mismatch was varied. To apply HFGMC to this thermal conductivity problem, the fiber and matrix constituent (rank three) property tensors, $\mathbf{Z}$ (see Eq. (8)), are simply set as diagonal, with the diagonal components equal to the isotropic constituent thermal conductivities. Then, upon solution, the (rank three) effective property tensor, $\mathbf{Z}^{*}$ (see Eq. (56)) will correspond to the effective thermal conductivity tensor of the composite.

Tang and Yu (2007) fixed the matrix thermal conductivity at 1 W/mK and varied the fiber thermal conductivity from 1 to 10,000 W/mK, resulting in a constituent thermal conductivity contrast ratio (CR = fiber thermal conductivity divided by matrix thermal conductivity) of 1 to 10,000. Herein, the HFGMC predictions have been compared to these results, along with the classical Christensen (1979) and Mori-Tanaka method (1973), which have also been extended to CR values less than one by varying the fiber thermal conductivity from 1 to 0.0001 W/mK. Tang and Yu's (2007) finite element model considered a fixed square fiber packing arrangement and fixed fiber volume fraction of 0.65, which have been adopted in the present HFGMC simulations. The HFGMC RUC, consisting of 102×102 subcells, is shown as an inset in Figure 2. Note that, in the present case, with square packed continuous fibers and isotropic constituents, the HFGMC effective thermal conductivity tensor exhibits transverse isotropy, and is thus diagonal with one non-zero component corresponding to the effective axial thermal conductivity and the remaining two non-zero components corresponding to the effective transverse thermal conductivity.

Figure 2 compares the HFGMC predictions for the effective transverse thermal conductivity to finite element results (Tang and Yu, 2007) and the classical predictions of Christensen's (1979) equation and the Mori-Tanaka (1973) method (based on the shear analogy) for varying constituent property contrast ratio (CR). All methods predict the same expected qualitative trend, with the effective transverse thermal conductivity saturating to a constant value as the contrast ratio becomes large or small. However, for CR > 1 (highly conductive fiber in insulative matrix), the classical methods (which correspond closely) saturate to a value 13 percent lower than that of the finite element model and HFGMC (which also correspond closely). At CR = 1, there is no mismatch, so the composite actually represents a monolithic material, and, as they must, all methods predict an effective transverse thermal conductivity of 1 W/mK. For CR < 1 (highly conductive matrix with insulative fiber), the classical methods now overpredict the effective transverse thermal conductivity, saturating to a value 16 percent higher than HFGMC. Recall that Tang and Yu (2007) considered only CR ≥ 1 in their finite element predictions.

As mentioned above, the HFGMC theory, like purely numerical approaches and in contrast to the classical methods, enables prediction of the local fields within the composite. Figure 3 presents a

comparison of the normalized local temperature and heat flux component fields predicted by HFGMC for the cases CR = 0.0001, CR = 10, and CR = 10,000 when the composite was subjected to a global (far-field) heat flux of $\bar{q}_2$ with $\bar{q}_1 = \bar{q}_3 = 0$. Note that the normalized temperature field magnitude scales linearly with the dimensions of the RUC, so these dimensions were set to 1 (i.e., $H = L = 1$, see Figure 1(b)). Therefore the plotted temperature fields are also normalized with respect to these dimensions and, for example, a plotted temperature gradient of 4.6 °C/(W/m²) over the RUC would correspond to a temperature gradient of 4.6×10⁻⁵ °C for an actual fiber spacing of 10 μm subjected to a far-field $\bar{q}_2 = 1$ W/mK. Noting that the scales associated with the CR = 0.0001 plots are vastly different that those associated with CR = 10 and CR = 10,000, it is clear that a much larger temperature gradient is induced when CR = 0.0001 due to the much lower effective transverse thermal conductivity (see Figure 2). In all three cases, the bottom boundary of the RUC is at a constant (reference) normalized temperature of 0 °C/(W/m²), whereas the top boundary of the RUC attains a constant normalize temperature equal to $-1/\kappa_T^*$ °C/(W/m²), where κ_T^* is the effective transverse thermal conductivity.
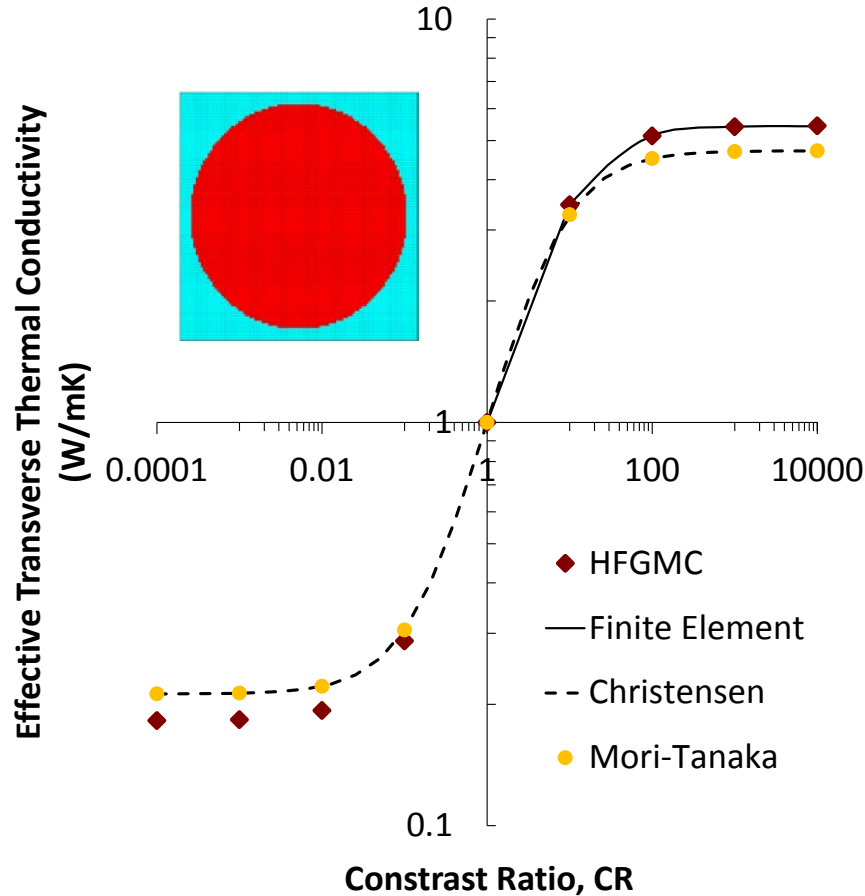

Figure 2.—Effective transverse thermal conductivity of a continuous composite with variable contrast ratio between the constituent thermal conductivities. HFGMC predictions are compared to finite element results (Tang and Yu, 2007) and the classical predictions of Christensen's (1979) equation and the Mori-Tanaka (1973) method. The HFGMC RUC is shown as an inset.
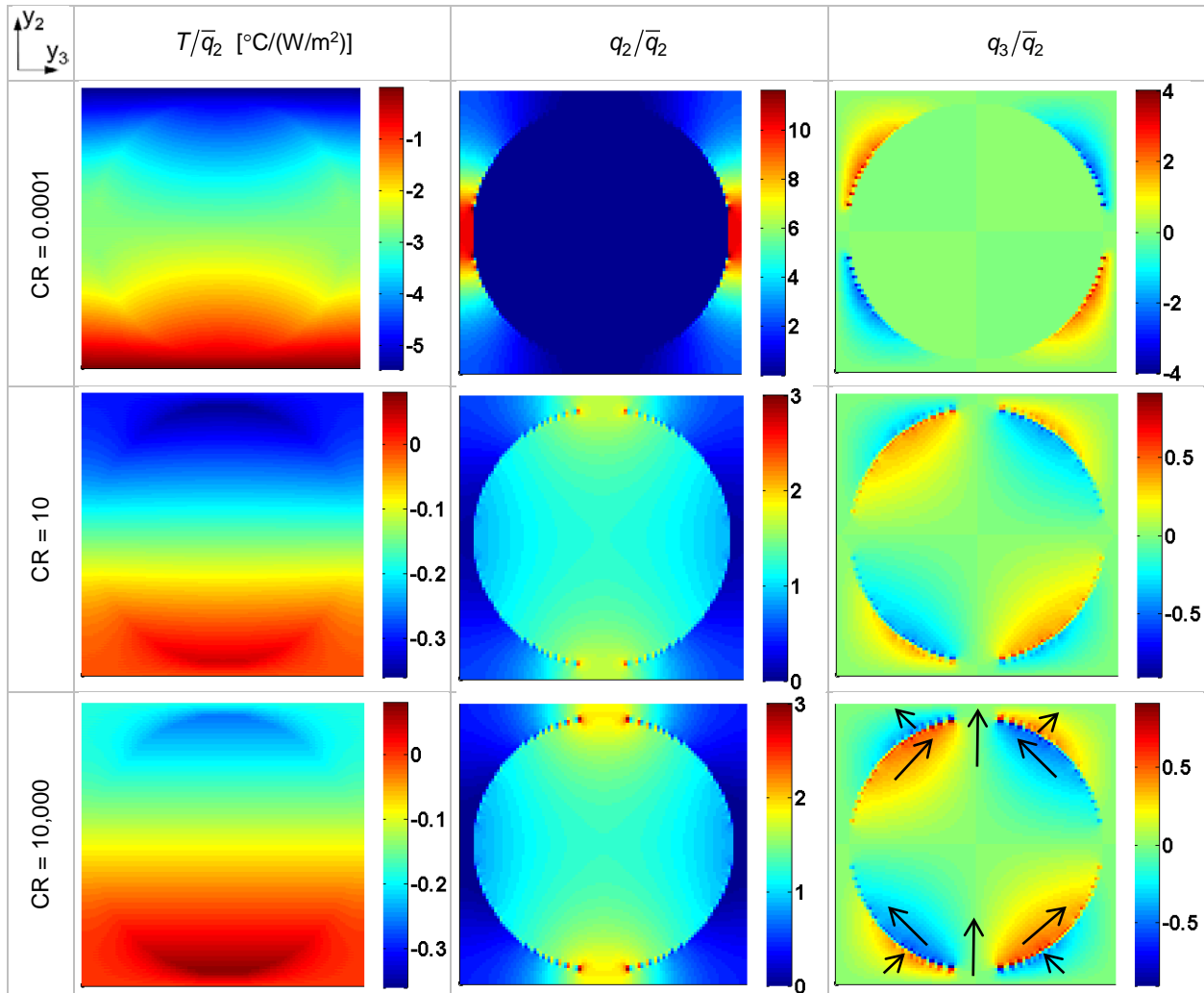
Figure 3.—Comparison of local normalized temperature and thermal flux component fields predicted by HFGMC for two extreme values and one moderate value of the contrast ratio (CR) between the constituent properties. A global heat flux component $\bar{q}_2$ was applied, with $\bar{q}_1 = \bar{q}_3 = 0$. Note that the fields for CR = 0.0001 are plotted on different scales.

Examining the $q_2/\bar{q}_2$ fields (center column Figure 3), which represent the local heat flux component in the direction of the applied global heat flux, it is clear that, for the case with CR = 0.0001, the heat flux is near zero in the fiber due to its very low thermal conductivity. Therefore the heat flow is forced around the fiber as it flows from the bottom of the RUC to the top (positive y_2-direction) in the opposite direction of the temperature gradient. Large heat flux concentrations are thus present at the pinch points between adjacent fibers at the right and left sides of the RUC. In contrast, for CR = 10 and CR = 10,000, the fiber has a very high thermal conductivity, and therefore most of the heat flow is through the fiber. However, because there is not a continuous path through the fiber in the transverse direction, the heat must be conducted through the lower thermal conductivity matrix to enter the top and bottom of the fiber. This leads to the high flux concentrations at the top and bottom of the RUC at the fiber/matrix interface, with higher concentrations for the higher concentration ratio case. The ramifications of these local q_2 heat flux concentrations, which necessarily correspond to local high temperature gradients, can be seen in the normalized temperature fields. Locally, the normalized temperature rises to a value higher than that of the

lower boundary (near the bottom of the RUC) and a value lower than the upper boundary (near the top of the RUC).

Finally, turning attention to the $q_3/\overline{q}_2$ fields, it is clear that this induced lateral heat flux is of significantly lower magnitude than the heat flux in the applied global heat flux direction. Furthermore, this induced lateral heat flux must sum to zero because the applied global lateral heat flux is zero. In all three cases, the $q_3/\overline{q}_2$ exhibits concentrations near the fiber matrix interface, reminiscent of the transverse shear stress distribution in a mechanical composite micromechanics problem. For the case with CR = 0.0001, again, the heat flux in the fiber is near zero because of its extremely low thermal conductivity. The $q_3/\overline{q}_2$ concentrations arise in the matrix as the heat flow is forced through the matrix around the fiber. In contrast, for CR = 10 and CR = 10,000, in which the fiber has a high thermal conductivity, not only are there lateral heat flux concentrations in the fiber, but also the lateral heat flux concentrations in the matrix are in the opposite directions compared to the CR = 0.0001 case. Now these matrix concentrations represent heat flow in to and out of the fiber (rather than around it), and once in the fiber, the heat is free to flow laterally to take full advantage of the volume of the high conductivity fiber. The arrows superimposed on $q_3/\overline{q}_2$ field for demonstrate the qualitative direction of the heat flow, as indicated by the HFGMC predictions.

3.2 Thermal Conductivity of a Composite With Varying Fiber Volume Fraction and Microstructure

Comparisons of HFGMC transverse thermal conductivity predictions have been made to experimental data from Thornburg and Pears (1965) (also reported by Springer and Tsai, 1967) for composites with two different contrast ratios between the fiber and matrix thermal conductivities: 666 and 4.4. Several different fiber packing arrangements, including hexagonal, square, random, and random pixelated, have been considered, and the predictions of Christensen's (1979) equation, the Mori-Tanaka (1973) method, and the Reuss approximation (assumption of constituents in series) are included as well, see Figure 5 and Figure 6.

Sample geometries of the HFGMC RUCs used in the analyses are shown in Figure 6. For the random fiber packing arrangement, 10 fibers were included in the RUC, with the fiber center locations chosen at random. While the fibers were not permitted to overlap, they were permitted to touch. For the random pixelated packing, the materials occupying each subcell were simply chosen at random according to the desired fiber volume fraction.

The normalized transverse thermal conductivity predicted by HFGMC is plotted vs. fiber volume fraction in Figure 4(a) and (b) for the 666 and 4.4 constituent contrast ratios, respectively. Consistent with Figure 2, the larger contrast ratio leads to much more spread among the model predictions. Interestingly, the Reuss approximation, which would be expected to be an extreme lower bound, matches the lower fiber volume fraction experimental data well for the 4.4 contrast ratio. Obviously, if the 4.4 contrast ratio were lowered in the simulations, the three lower fiber volume fraction experimental data points could be matched with all models aside from Reuss. However, the fourth (0.60 fiber volume fraction) data point would then not be matched. For the larger 666 contrast ratio case, the Reuss results form a lower bound as expected.

Focusing on Figure 4(a), the simple Reuss approximation provides a lower bound, while the classical Christensen (1979) equation and the Mori-Tanaka (1973) method are in close agreement, also under predicting the experimental data. Of the HFGMC predictions, the hexagonal packed RUC provides the closest prediction to these classical methods. This is to be expected as the hexagonal packing geometry maximizes the separation between the fibers, much like the geometry associated with Christensen and Mori-Tanaka approaches. Note that there is some small deviation between the effective thermal conductivities predicted for the two transverse directions in the case of the hexagonal fiber packing geometry, which becomes more pronounced as the fiber volume fraction increases and the fibers become closer spaced. The

square fiber packing provides identical predictions in the two transverse directions that are somewhat greater than those of the hexagonal packing arrangement and closer to the experimental results. This is due to the fact that, at a given fiber volume fraction, the distance between the high conductivity fibers is always smaller in the case of the square fiber packing.
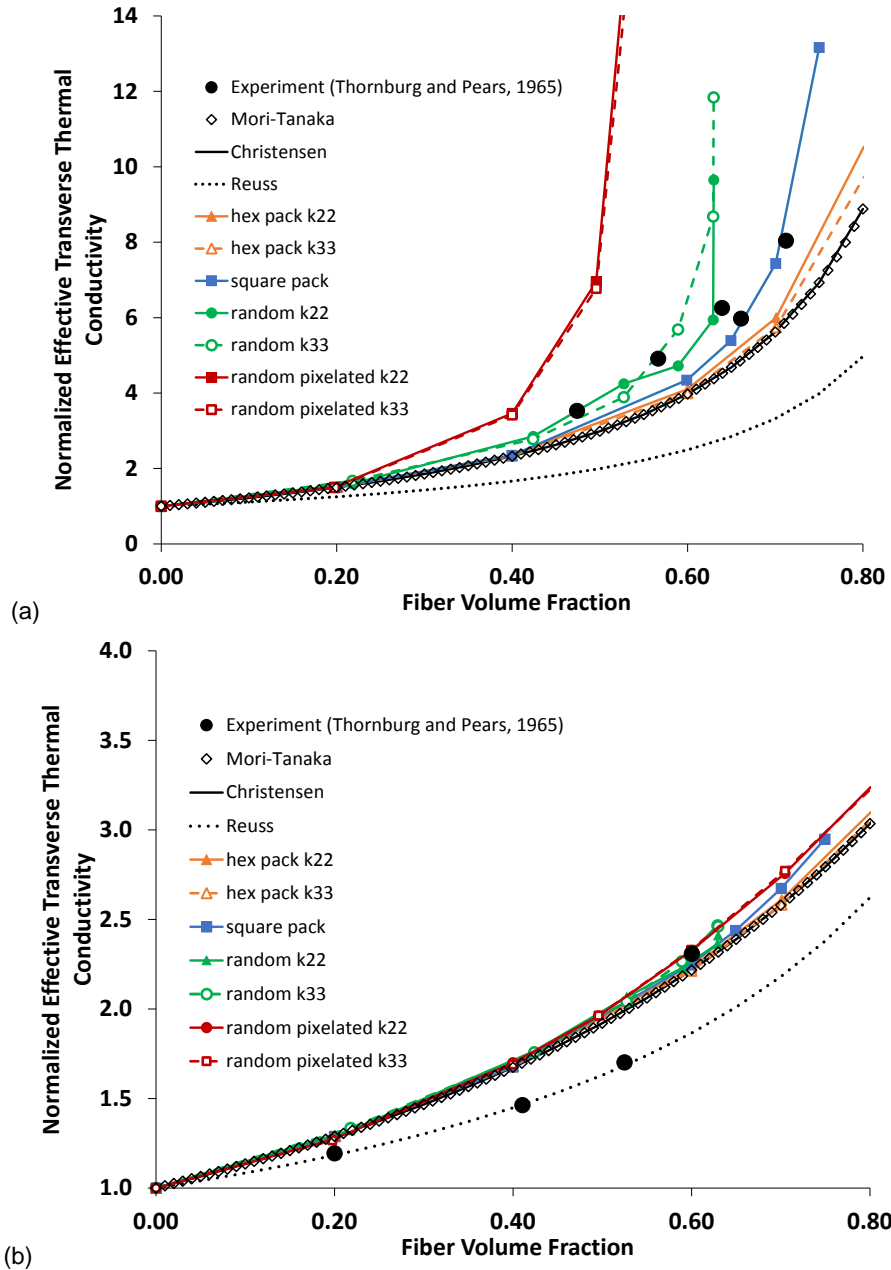

(a)

(b)

Figure 4.—Normalized effective transverse thermal conductivity as a function of fiber volume fraction for constituent thermal conductivity contrast ratio of (a) 666 and (b) 4.4. HFGMC predictions with various fiber packing arrangements are compared to experimental data (Thornburg and Pears, 1965), the Reuss approximation, and the classical predictions of Christensen's (1979) equation and the Mori-Tanaka (1973) method.
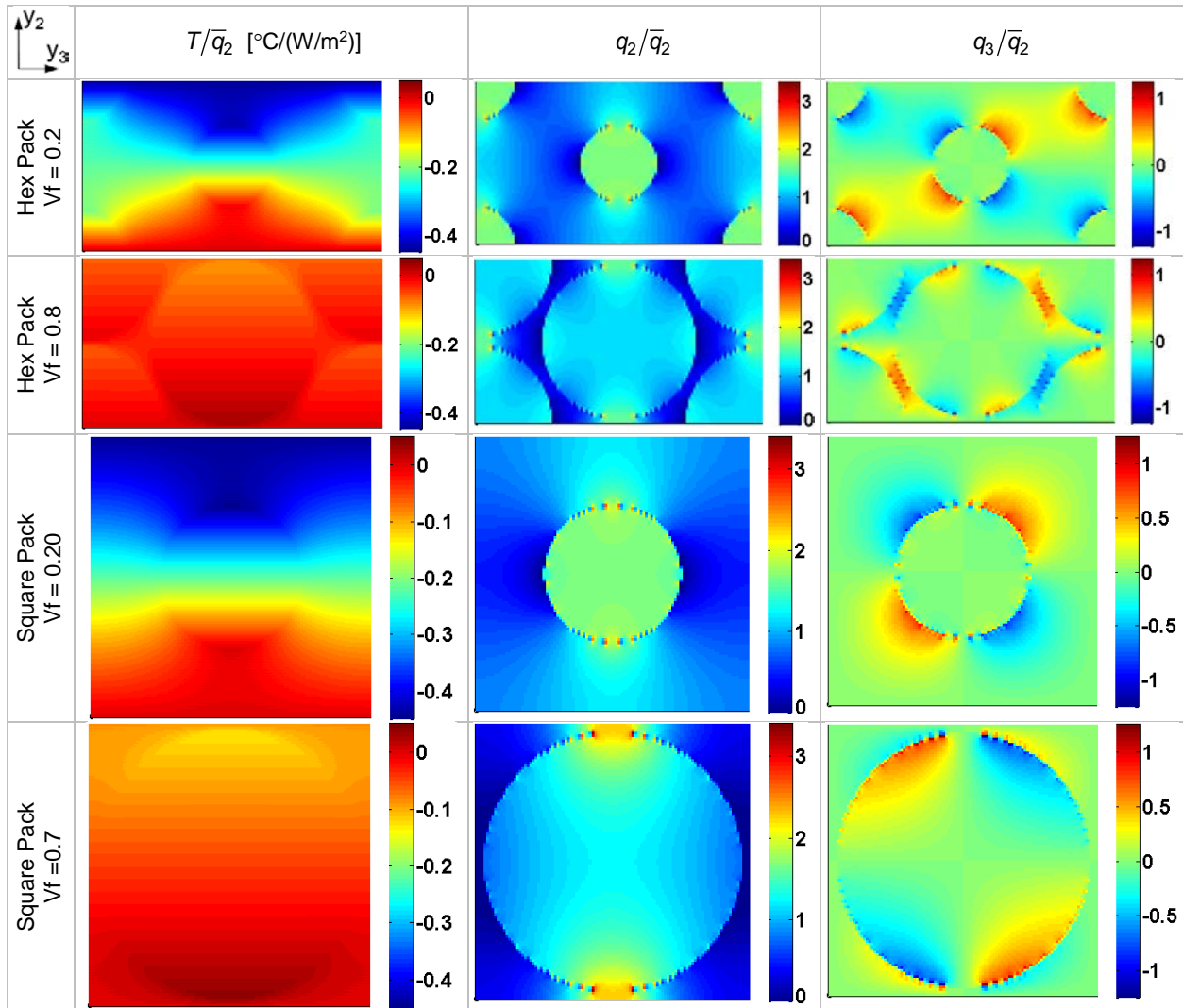
Figure 5.—Comparison of local normalized temperature and thermal flux component fields for hexagonal and square fiber packing arrangements predicted by HFGMC for high and low fiber volume fraction (Vf) composites with a 666 constituent thermal conductivity contrast. A global heat flux component $\overline{q}_2$ was applied, with $\overline{q}_1 = \overline{q}_3 = 0$.

The random fiber packing results in the two transverse directions are quite different above a fiber volume fraction of approximately 0.55. This is near the point where many fibers within the RUC are beginning to touch, and thus near the so-called percolation threshold (the point at which there is a continuous fiber path through the RUC, c.f. Devpura et al., 2001). This difference also indicates that, at these higher volume fractions, the RUC containing 10 fibers is not sufficient to truly represent the bulk material (i.e., it is not a statistical representative volume element (RVE)). This is further supported by the fact that the random fiber predictions match the experimental data quite well up to a fiber volume fraction of approximately 0.64, and then quickly deviate as the percolation threshold is reached. A larger RUC, with more fibers would be expected to reach the percolation threshold at a higher fiber volume fraction (due to the greater likelihood of gaps disrupting the continuous fiber path), enabling better agreement with experiment at the higher fiber volume fractions.
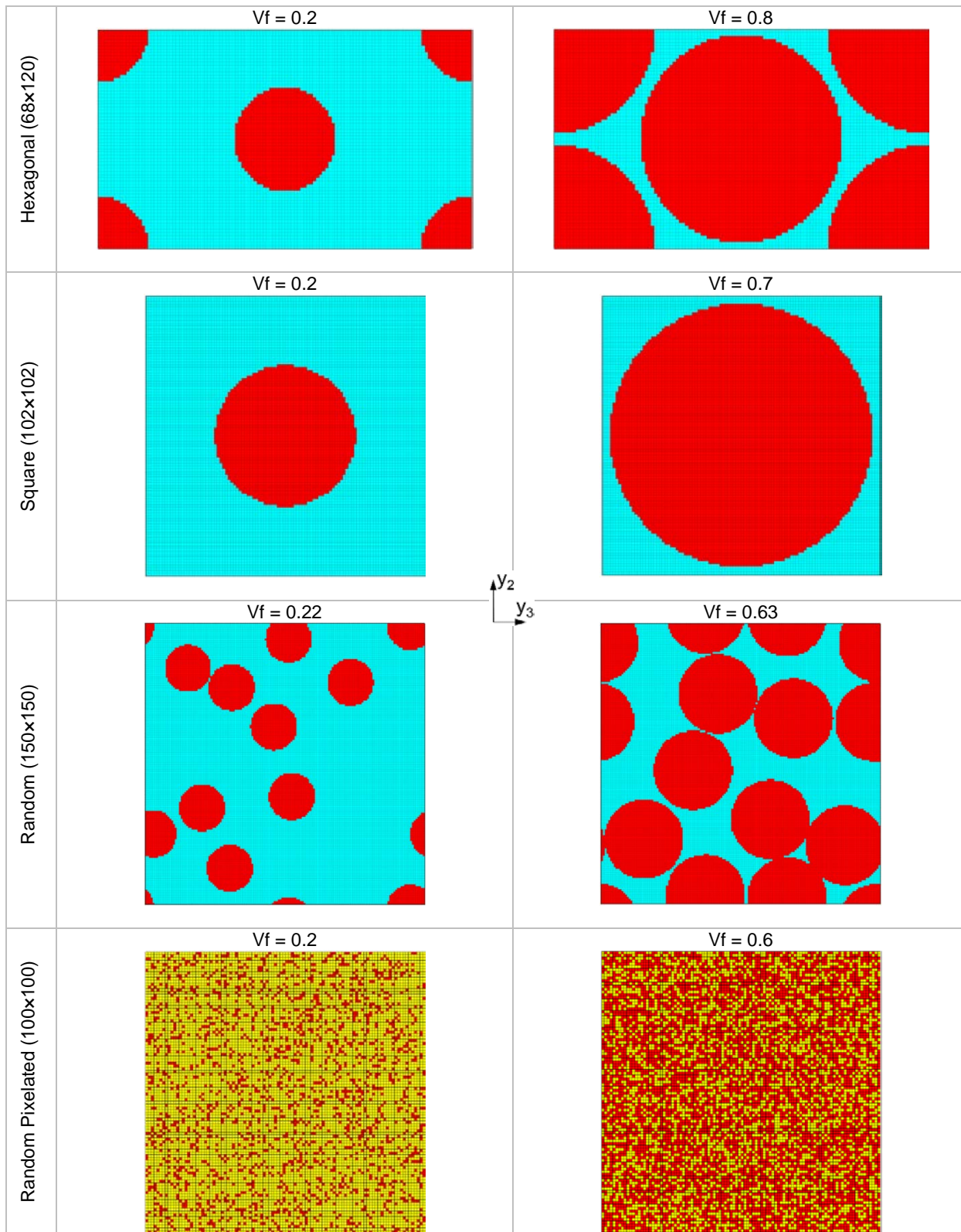
Figure 6.—Sample HFGMC RUCs with different fiber packing arrangements employed in the prediction of the transverse thermal conductivities of composites with constituent thermal conductivity contrast ratios of 666 and 4.4. In all cases, the red color indicates the fiber material.

The random pixelated microstructure provided the highest predictions of the composite transverse thermal conductivity. The predictions in the two transverse directions were in good agreement, indicating that the RUC size was sufficient, but the fact that the percolation threshold is reached at a fiber volume fraction that is clearly too low compared to the experimental data indicates that this type of geometry is inappropriate for a problem with such large constituent property mismatch. Further, it is an indication that the fiber shape and fiber packing arrangement is important as the pixelated geometry allows adjacent pixels occupied by the high conductivity fiber to have a great deal of contacted surface area. In contrast, touching circular fibers have a relatively low degree of surface contact. Examining Figure 4(b), the shortcomings of the pixelated microstructure are largely muted when the constituent thermal conductivity mismatch is low.

Figure 5 compares the normalized local fields for hexagonal and square fiber packing arrangements for cases with widely (fiber volume fraction = 0.2) and closely (fiber volume fractions = 0.8 and 0.7, respectively) spaced fibers. For widely spaced fibers, which represents a dilute case, the fields associated with hexagonal and square packing are similar (which results in the similar effective thermal conductivity, as shown in Figure 4). As the fibers become more closely spaced, the high conductivity fibers interact, resulting in high heat flux concentrations in the low conductivity matrix located between the closely spaced fibers. The arrangement of the closely spaced fibers then has a significant impact, not only on the local fields, but also on the effective thermal conductivity at these higher fiber volume fractions. The fact that the square packing arrangement leads to greater heat flux in the high conductivity fiber than does the hexagonal packing arrangement (given the identical applied heat flux) causes the effective thermal conductivity of the square packing arrangement to be higher, as indicated in Figure 4.

For the random microstructural geometries considered, it is more instructive to examine the heat flux magnitude ($\sqrt{q_2^2 + q_3^2}$), as opposed to the components, as this reveals the path taken by the heat flow through the random RUC geometry. As such, Figure 7 shows the heat flux magnitude for high and low fiber volume fraction HFGMC simulations with random fiber packing and pixelated microstructure. For the random fiber packing, four RUCs have been tiled to better illustrate the path of the heat flow in the simulation. For this same reason, the upper bounds of the colorbar scales have been set low, with all dark red color representing heat flux magnitude at or greater than the displayed upper bound.

In the case of the random fiber packing arrangements, it is clear that the heat flow follows a low resistance path through fibers (since their conductivities are 666 times greater than the matrix) that are relatively closely spaced in the direction of the applied global heat flux ($\overline{q}_2$). For low fiber volume fraction, the path is forced through many low thermal conductivity matrix regions, but the heat flow still follows a locally high fiber density path. In contrast, for the high fiber volume fraction, there is a path of nearly touching fibers through the RUC (see Figure 6). Matrix that is not directly between fibers along this path experiences very low heat flux. In the case of the pixelated microstructures, the low fiber volume fraction geometry exhibits much more uniform heat flux magnitude, whereas the high fiber volume fraction geometry shows a clear network of high heat flux material. The associated continuous path of high thermal conductivity material through the RUC indicates that this geometry is indeed above the percolation threshold. Finally, in the case of the high fiber volume fraction composite with random circular fiber packing arrangement, the fact that the heat flow is still forced through some sizeable regions of low conductivity matrix between the fibers (see Figure 6) results in much lower effective conductivity than the corresponding pixelated case (see Figure 4), with its continuous high conductivity path.
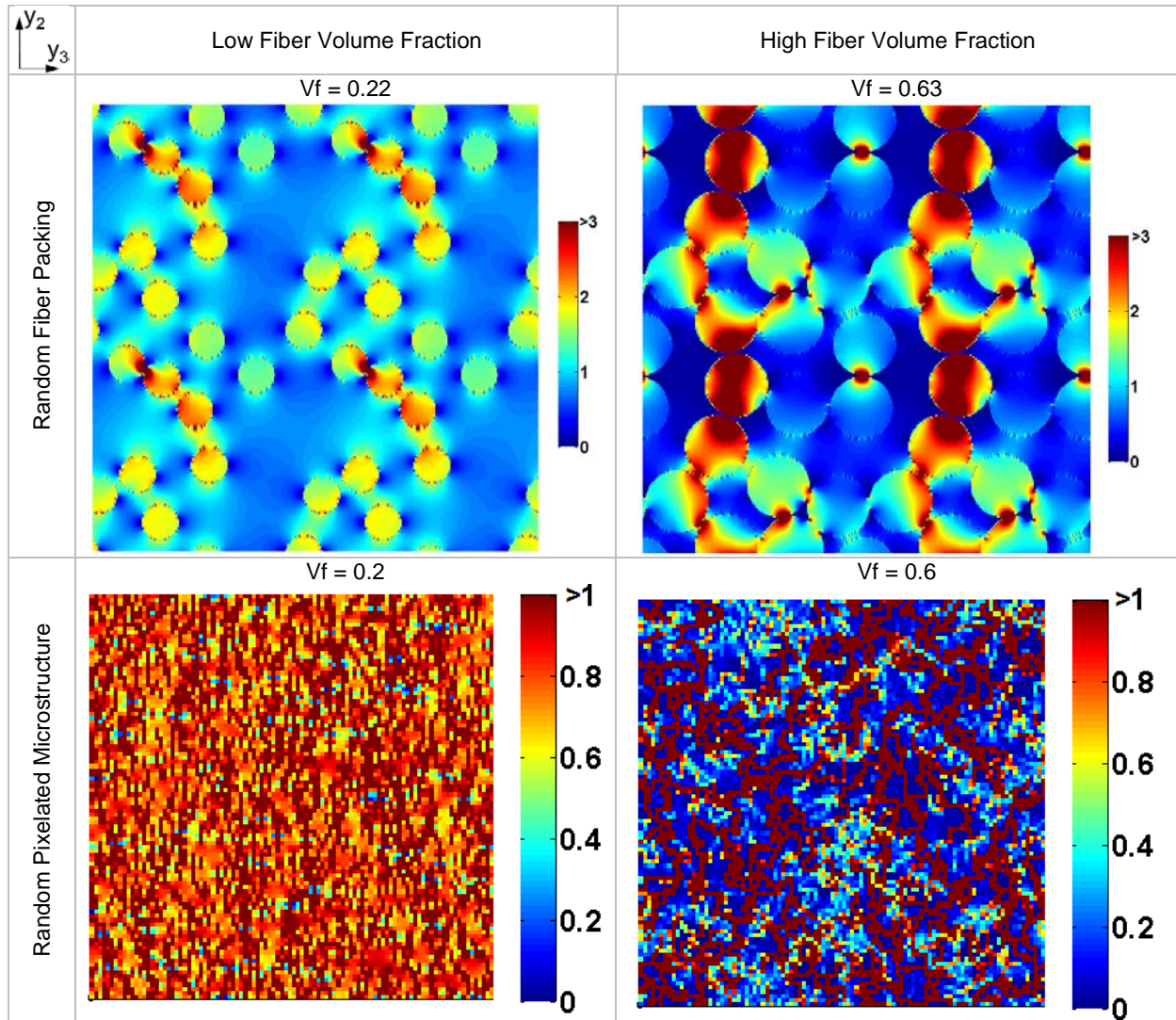
Figure 7.—Comparison of local normalized heat flux magnitude fields for random fiber packing arrangements and random pixelated geometries predicted by HFGMC for high and low fiber volume fraction (Vf) composites with a 666 constituent thermal conductivity contrast. A global heat flux component $\bar{q}_2$ was applied, with $\bar{q}_1 = \bar{q}_3 = 0$. Note that, for the random fiber packing arrangements, four RUCs have been tiled.

3.3 Electric Permittivity of a Discontinuous Composite With Varying Fiber Volume Fraction

The effective electric permittivity predictions of HFGMC have been compared to the boundary integral equation (BIE) approach of Sarini et al. (1996), along with various analytical approximations, for two discontinuously reinforced composite configurations. In accordance with these authors, the effective dielectric constants, which are the unitless electric permittivities relative to a vacuum, were predicted as a function of fiber volume fraction. The microstructures considered both involve cylindrical inclusions in a parallelepiped RUC, one in which the cylindrical inclusion is long (aspect ratio of 8), and the other with a short, disk-like inclusion (aspect ratio 0.1); see Sarini et al. (1996) Fig 2c and d. To facilitate maintaining the inclusion aspect and RUC ratios assumed by Sarini et al. (1996) with varying fiber volume fraction, in HFGMC, these microstructures have been approximated with the simplest RUC possible. This consisted of a 3×3×3 subcell RUC, in which the center subcell represented the inclusion. The subcell dimensions were

then altered to achieve the correct aspect ratios and fiber volume fractions. The constituent dielectric constants were 3 and 1, respectively, for the inclusion and the matrix materials.

Figure 8 compares the effective dielectric constant predictions of HFGMC to the results presented by Sarini et al. (1996). In Figure 8(a) and (b), the predictions for the long (aspect ratio of 8) cylindrical inclusion are shown. In the axial direction, the HFGMC predictions fall within the bounding equation results, attributed by Sarini et al. (1996) to Van Beek (1967). The BIE predictions follow the same trend, but are somewhat higher, falling just outside the upper bound of Van Beek (1967). In the transverse directions, the BIE and HFGMC predictions are nearly coincident and slightly above results attributed by Sarini et al. (1996) to Rayleigh's equation.

Figure 8(c) and (d) compare the BIE and HFGMC predictions for the short, disk-like inclusion (aspect ratio of 0.1), with the Voigt (constituents in parallel) and Reuss (constituents in series) approximations, which should serve as upper and lower bounds. The BIE results are again somewhat higher than the
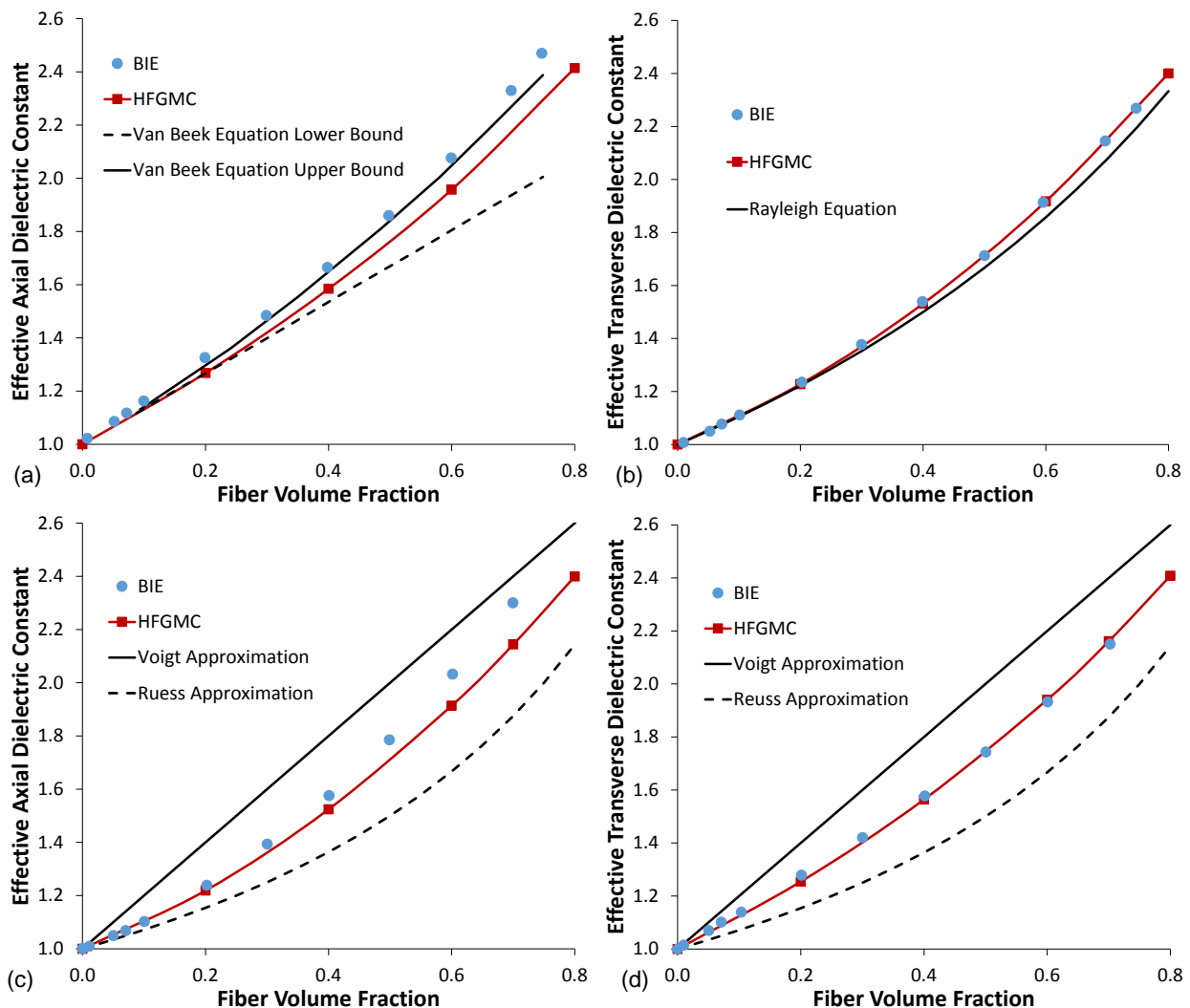

Figure 8.—Composite effective dielectric constants as a function of fiber volume fraction predicted by HFGMC, the boundary integral equation (BIE) approach of Sarini et al. (1996), and several analytical expressions presented by Sarini et al. (1996) for (a) long cylindrical inclusion (axial direction), (b) long cylindrical inclusion (transverse direction), (c) short cylindrical (disk-like) inclusion (axial direction), (d) short cylindrical (disk-like) inclusion (transverse direction).

HFGMC results in the axial direction, while, in the transverse direction, the BIE and HFGMC results are in close agreement. In both directions, the BIE and HFGMC approaches are within the bounds represented by the Voigt and Reuss approximations.

3.4   Thermal Conductivity and Electric Permittivity of a Composite With a Continuous, Tortuous, Inclusion

A particularly challenging microstructure for a micromechanics model involves a continuous reinforcing phase with a tortuous path. An example of such a microstructure, with varying fiber volume fraction, is shown in Figure 9. Similar to a bent wire, the reinforcing phase changes direction by 90 degrees within the microstructure, but is continuous, even across the periodic boundaries, in the y_3-direction. If the reinforcing phase exhibits high properties, while the properties of the matrix material are low, the flux must follow the tortuous path introduced by the microstructure, which tightly links the effective properties to the microstructure. Obviously, classical methods, which do not explicitly consider the microstructure, would be expected to give poor approximations of the properties of such a microstructure.
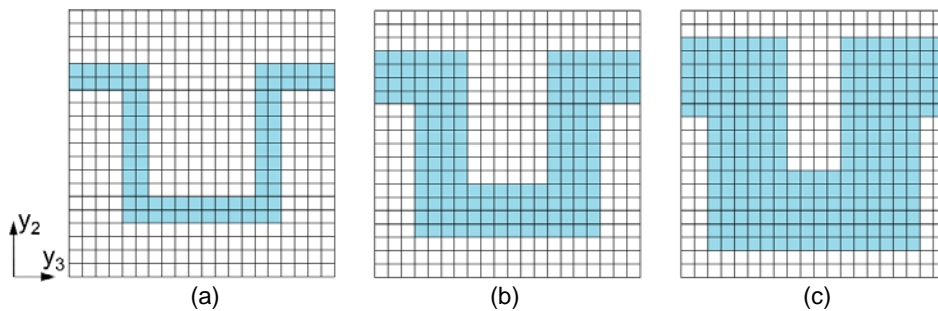

Figure 9.—Composite microstructures featuring a continuous inclusion with a tortuous path. (a) Volume fraction of 0.2, (b) volume fraction of 0.4, (c) volume fraction of 0.6.
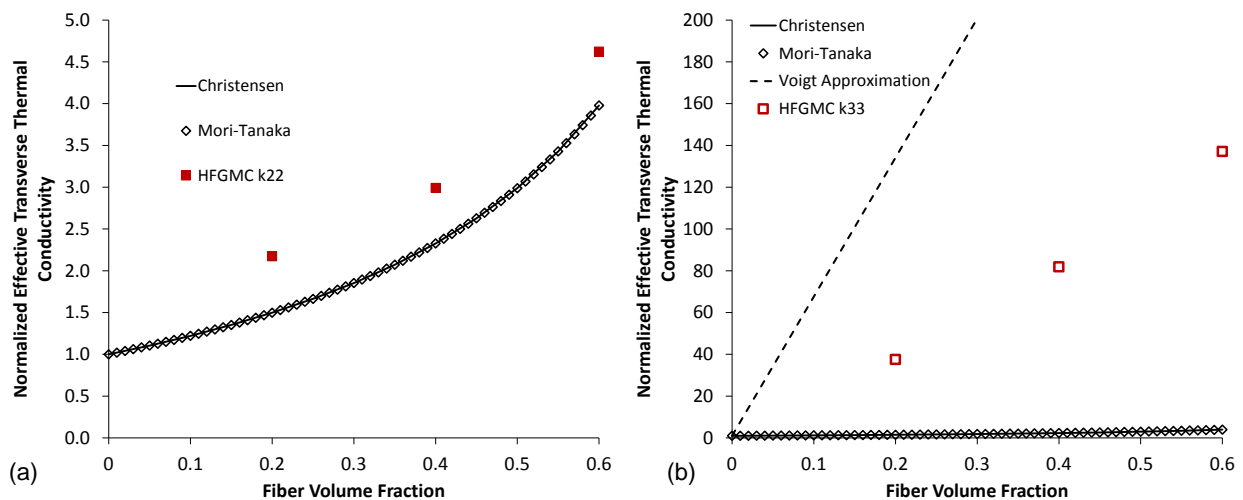

Figure 10.—Normalized effective transverse thermal conductivity for a composite with a continuous, tortuous reinforcement as a function of fiber volume fraction for constituent thermal conductivity contrast ratio of 666. (a) In the discontinuous y_2-direction and (b) in the continuous y_3-direction. HFGMC predictions are compared to the classical predictions of Christensen's (1979) equation and the Mori-Tanaka (1973) method, as well as the Voigt approximation.
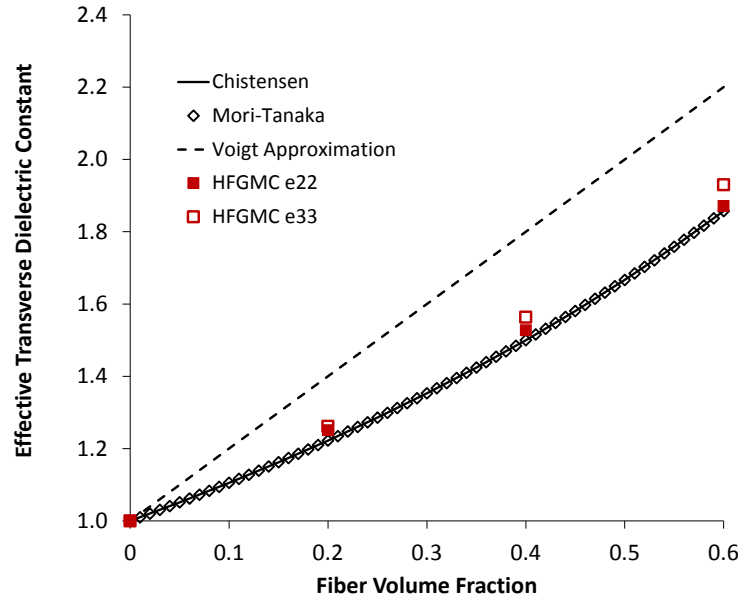
Figure 11.—Effective transverse dielectric constant for a composite with a continuous, tortuous reinforcement as a function of fiber volume fraction for constituent dielectric contrast ratio of 3. HFGMC predictions are compared to the classical predictions of Christensen's (1979) equation and the Mori-Tanaka (1973) method, as well as the Voigt approximation.

To examine the impact of the continuous, tortuous microstructure on the HFGMC predictions, a thermal conductivity problem with constituent property mismatch ratio of 666 (from section 3.2), as well as an electric permittivity problem with constituent property mismatch ratio of 3 (from section 3.3), have been considered. The three microstructures shown in Figure 9 were used. Note that the inclusion microstructures are continuous and straight in the y_1-direction, discontinuous and layered in the y_2-direction, and continuous and tortuous in the y_3-direction.

Figure 10 shows that, for the thermal conductivity problem with large mismatch between the constituent properties, HFGMC predicts a tremendous (factor of 20 to 30) difference between the effective thermal conductivity in the discontinuous y_2-direction and the continuous but tortuous y_3-direction (see Figure 9). This is expected as the microstructures are intended to provide a continuous conduction path through the microstructure in the y_3-direction. The classical Christensen and Mori-Tanaka approaches, which lack the detailed information about the microstructure, obviously cannot capture the effect of the continuous, tortuous path on the effective thermal conductivity. As shown in Figure 10, treating the microstructure as continuous without accounting for the tortuosity with the Voigt approximation significantly overpredicts the effective thermal conductivity compared to HFGMC.

Figure 11 shows the predictions for the effective dielectric constant of the same continuous, tortuous microstructures for the case where the constituent property mismatch ratio is only 3. Due to this much lower property mismatch ratio, the impact of the tortuosity on the predictions is muted, and the spread among the predictions is much less.

Figure 12 shows the local heat flux component and magnitude fields predicted by HFGMC for the thermal problem with the large constituent property mismatch ratio, wherein the composite was subjected to a global heat flux in the y_3-direction. Clearly, the HFGMC theory is able to capture the correct physics of this problem, where the heat flux switches locally between the q_3 component and the q_2 component as the heat flows along the tortuous path of the high thermal conductivity material through the microstructure.

It is interesting to note that, even within the high thermal conductivity material, the heat flux naturally follows efficiently, concentrating along the shortest path across the RUC.

3.5 Thermal Conductivity and Electric Permittivity of a Woven Composite

A technologically significant example of a composite with a tortuous reinforcement is a woven composite. As shown in Figure 13, the undulating fiber yarns (tows) in a plain weave composite are continuous through the RUC, but their paths are tortuous as they pass over each other. The effective thermal conductivity and the effective dielectric constant of this plain weave composite have been predicted for constituent property mismatch ratios of 666 (κ_f = 1000 W/mK, κ_m = 1.5 W/mK) and 3 (ε_f = 3, ε_m = 1), respectively. The dimensions are as follows: w_{yarn} = 4.8 mm, $w_{\text{cross-over}}$ = 0.96 mm, h_{yarn} = 0.3613 mm, h_{coating} = 0.14 mm, which leads to a yarn volume fraction of 0.6, with the remainder of the composite occupied by pure matrix material. In the yarn cross-over regions, and angle of $\tan^{-1}(h_{\text{yarn}}/w_{\text{cross-over}})$ = 20.6° was employed. The effective properties of the yarns were determined using a 102×102 subcell HFGMC RUC with square fiber packing arrangement and a fiber volume fraction of 0.6. This resulted in an effective
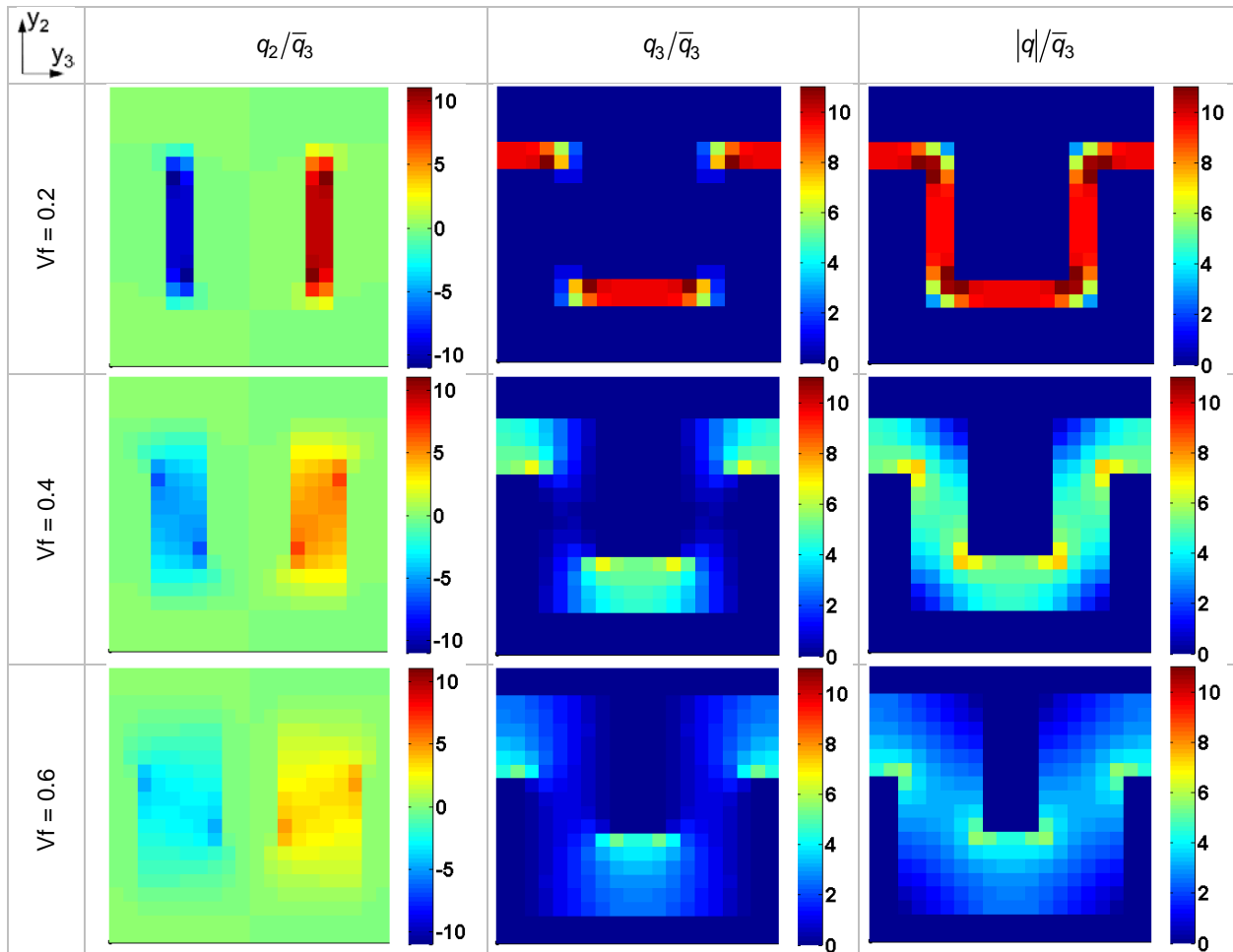

Figure 12.—Comparison of local normalized thermal flux component and magnitude fields for the continuous, tortuous microstructure predicted by HFGMC for 0.2, 0.4, and 0.6 volume fraction (Vf) composites with a 666 constituent thermal conductivity contrast. A global heat flux component $\bar{q}_3$ was applied, with $\bar{q}_1 = \bar{q}_2 = 0$.
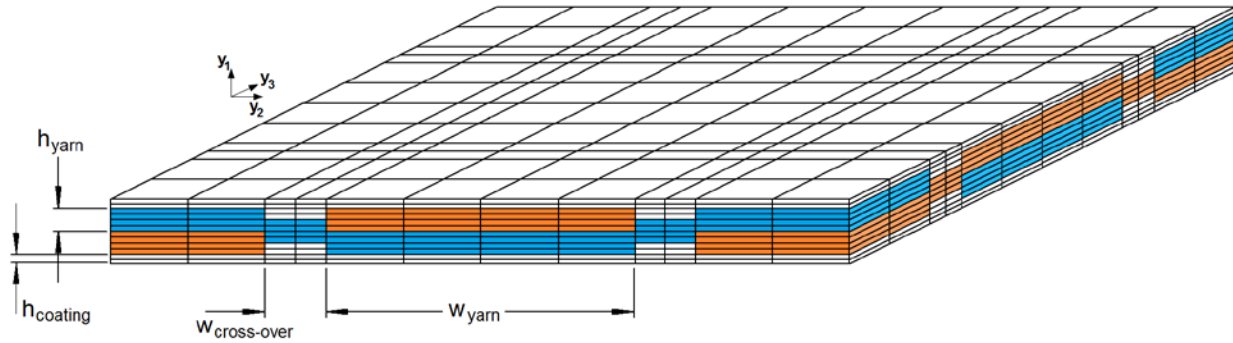
Figure 13.—Plain weave composite RUC modeled by HFGMC. The blue and orange subcells represent the fiber yarns (tows) oriented in the two in-plane direction, while the white subcells contain the pure matrix material.

TABLE 1.—EFFECTIVE THERMAL CONDUCTIVITIES AND
DIELECTRIC CONSTANTS PREDICTED BY HFGMC
FOR THE PLAIN WEAVE COMPOSITE

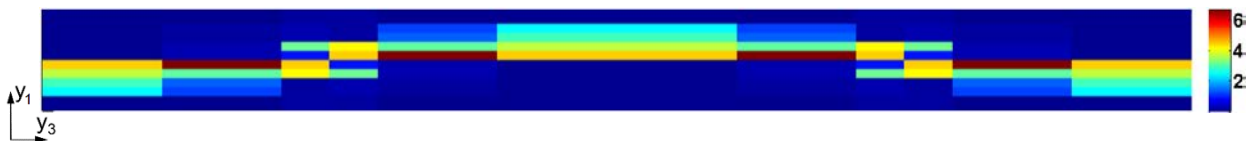|	
In-plane thermal conductivity, W/mK 42.35
Through-thickness thermal conductivity, W/mK 3.00
In-plane dielectric constant 1.60
Through-thickness dielectric constant..1.41

Figure 14.—Local normalized thermal flux magnitude field for the plain weave composite plotted along the center of a yarn oriented in the y_3-direction predicted by HFGMC with a 666 constituent thermal conductivity contrast. A global heat flux component $\bar{q}_3$ was applied, with $\bar{q}_1 = \bar{q}_2 = 0$.

yarn axial and transverse thermal conductivity of 599.6 and 6.517 W/mK, respectively, and an effective yarn axial and transverse dielectric constant of 2.198 and 1.8677, respectively. These effective yarn properties were then used as the subcell properties in the HFGMC analysis, with appropriate orientation per subcell, to correctly represent the RUC geometry shown in Figure 13. The overall fiber volume fraction of the woven composite is 0.36.

The predicted effective thermal conductivities and dielectric constants of the woven composite are given in Table 1. As expected, the composite effective thermal conductivity is significantly higher in the in-plane direction, which contains the continuous fiber yarns, compared to the through-thickness direction. The effective dielectric constants in the two directions are much closer because the mismatch in the dielectric constants of the fiber and matrix constituent materials was much smaller (3 vs. 666).

The predicted local heat flux magnitude within a yarn oriented in the y_3-direction is plotted in Figure 14, in response to an applied global heat flux in the y_3-direction (with other global heat flux components kept at zero). Clearly, the heat flow is along the high thermal conductivity fiber yarn, with the highest concentration near the midplane of the composite, allowing the heat flow to minimize the tortuosity of its flow path.

4.0   Conclusions

The HFGMC micromechanics theory has been extended to model physical phenomena governed by vector constitutive laws such as thermal and electrical conductivity, electrical permittivity, magnetic permeability, and diffusion. A general form of the three-dimensional HFGMC theory applicable to any of these physics within a periodic composite material has been presented, enabling prediction of the effective properties of composites with arbitrary periodic microstructures, as well as the local fields within the composite. The extended HFGMC theory was applied to thermal conductivity and electrical permittivity problems of various continuous and discontinuous composites that have been analyzed in the literature. Comparisons were made to the results of analytical approximations, classical methods, numerical approaches, and experimental test results. The effective properties predicted by HFGMC compare favorably with the test data and numerical models, while they are clearly more accurate than the classical methods and analytical approximations. Further, the availability of the local fields predicted by HFGMC provides clear explanations for the trends observed in the effective property predictions and would be useful for the design of a given microstructure to achieve a given performance metric.

The presented results clearly show that discrepancy between HFGMC and the simpler methods grows as mismatch ratio between the fiber and matrix constituent properties increases and as the composite microstructural geometry becomes more complex (i.e., directionally coupled). The geometric complexity of the microstructure was addressed by examining regular fiber packing arrangements (hexagonal and square packing), as well as random microstructures, as a function of fiber volume fraction. As the fiber volume fraction increases, the so-called percolation threshold, where a continuous path within the reinforcement phase through the entire microstructure, is approached. While the HFGMC approach is able to predict the percolation threshold, such conditions challenge the simpler methods that do not explicitly account for the microstructure. Likewise, microstructures containing a continuous, tortuous reinforcement phase cannot be accurately modeled by the simpler methods as the local path of the reinforcement phase dictates the local flux and thus the effective properties. HFGMC predictions for such microstructures show that the theory correctly captures these physics. The technologically relevant application to a woven composite, whose fiber yarns follow a continuous, tortuous path, was addressed as a final demonstration of the enhanced HFGMC's capabilities.

It has been observed that the bonding between the fibers and matrix in composite materials can be imperfect. In the context of thermal conductivity, such imperfect interfaces have been investigated in micromechanical models by Dunn and Taya (1993), Duan and Karihaloo (2007), Nan et al. (1997) and Hashin (2001). The present HFGMC micromechanical method, derived for perfectly bonded composite materials governed by vector constitutive laws, can be easily generalized to include the effects of weak bonding between the constituents. Such generalizations, in the context of the mechanical micromechanics problem, involve introduction of a traction-separation law at the fiber/matrix interface and have been presented by Aboudi (1987), Bednarcyk and Arnold (2002), Bednarcyk et al. (2004) and Aboudi et al. (2013) and will be addressed in the future.

References

Aboudi, J. (1987) "Damage in composites—modeling of imperfect bonding" Composites Science and Technology 28, 103–128.

Aboudi et al. (2013) Micromechanics of Composite Materials A Generalized Multiscale Analysis Approach, Elsevier, Oxford, UK.

Avila, H.A., Reboredo, M.M., Parra, R., and Castro, M.S. (2015) "Dielectric permittivity calculation of composites based on electrospun barium titanate fibers" Materials Research Express 2, 045302.

Bednarcyk, B.A. and Arnold, S.M. (2002) "Transverse tensile and creep modeling of continuously reinforced titanium composites with local debonding" International Journal of Solids and Structures 39, 1987-2017.

Bednarcyk, B.A., Arnold, S.M., Aboudi, J., and Pindera, M.-J. (2004) "Local field effects in titanium matrix composites subject to fiber-matrix debonding" International Journal of Plasticity 20, 1707-1737.

Chmielewski, M. and Wegelewski, W. (2013) "Comparison of experimental and modelling results of thermal properties in Cu-AlN composite materials" Bulletin of the Polish Academy of Sciences Technical Sciences 61, 507-514.

Christensen, R.M. (1979) Mechanics of Composite Materials, Krieger, Malabar, FL.

Devpura, A., Phelan, P.E., and Prasher, R.S. (2001) "Size effects on the thermal conductivity of polymers laden with highly conductive filler particles" Microscale Thermophysical Engineering 5, 177-189.

Dinulovic, M. and Rasuo, B. (2009) "Dielectric properties modeling of composite materials" FME Transactions 37, 117-122.

Duan, H.L. and Karihaloo, B. L. (2007) "Effective thermal conductivities of heterogeneous media containing multiple imperfectly bonded inclusions" Phys. Rev. B 75, 064206.

Dunn, M.L. and Taya, M. (1993) "The effective thermal conductivity of composites with coated reinforcement and the application to imperfect interfaces" J. Appl. Phys. 73, 1711-1722.

Floury, J., Carson, J, and Pham, Q.T. (2008) "Modelling thermal conductivity in heterogeneous media with the finite element method" Food and Bioprocess Technology 1, 161-170.

Hamilton, R.L. and Crosser, O.K. (1962) "Thermal conductivity of heterogeneous two-component systems" Ind. Eng. Chem. Fundamen. 1, 187–191.

Haj-Ali, R., Zemer, H., El-Hajjar, R., and Aboudi, J. (2014) "Piezoresistive fiber-reinforced composites: A coupled nonlinear micromechanical-microelectrical modeling approach" International Journal of Solids and Structures 51, 491-503.

Hashin, Z. (1972) Theory of Fiber Reinforced Materials, NASA CR-1974.

Hashin, Z. (2001) "Thin interphase/imperfect interface in conduction" J. Appl. Phys. 89, 2261-2267.

Hatta, H. and Taya, M. (1985) "Effective thermal conductivity of a misoriented short fiber composite" J. Appl. Phys. 58, 2478-2486.

Islam, Md.R. and Pramila, A. (1999) "Thermal conductivity of fiber reinforced composites by the FEM" Journal of Composite Materials 33, 1699- 1715.

Kumar, S., Bhoopal, R.S., Sharma, P.K., Beniwal, R.S., and Singh, R. (2011) "Nonlinear effect of volume fraction of inclusions on the effective thermal conductivity of composite materials: A modified Maxwell model" Open Journal of Composite Materials 1, 10-18.

Mori, T. and Tanaka, K. (1973) "Average stress in matrix and average energy of materials with misfitting inclusions" Acta Metall. 21, 571-574.

Murthy, P.L.N. and Pineda, E.J. (2016) "Tool for Generation of MAC/GMC Representative Unit Cell for CMC/PMC Analysis" NASA/TM—2016-219127.

Nan, C.-W., Birringer, R., Clarke, D.R., and Gleiter, H. (1997) "Effective thermal conductivity of particulate composites with interfacial thermal resistance" J. Appl. Phys. 81, 6692-6699.

Pietrak, K. and Wisniewski, T.S. (2015) "A review of models for effective thermal conductivity of composite materials" Journal of Power Technologies 95, 14-24.

Sarini, B., Krahenbuhl, L., Beroual, A., and Brosseau, C. (1996) "Effective dielectric constant of periodic composite materials" J. Appl. Phys. 80, 1688-1696.

Springer, G.S. and Tsai, S.W. (1967) "Thermal conductivities of unidirectional materials" Journal of Composite Materials 1, 166-173.

Tang, T. and Yu, W. (2007) "A variational asymptotic micromechanics model for predicting conductivities of composite materials" Journal of Mechanics of Materials and Structures 2, 1813-1830.

Thornburg, J.D. and Pears, C.D. (1965) "Prediction of the thermal conductivity of filled and reinforced plastics" ASME Paper 65-WA/HT-4.

Van Beek, L.K.H. (1967) "Dielectric behavior of heterogeneous systems" Progress in Dielectrics 7, 69-114.